Red blood cell membrane-coated functionalized Cu-doped metal organic framework nanoformulations as a biomimetic platform for improved chemo-/chemodynamic/photothermal synergistic therapy

Luping Ren [a,b], Yanfang Sun [c,*], Junhao Zhang [a,b], Lei Nie [d], Amin Shavandi [e], Khaydar E. Yunusov [f], Uladzislau E. Aharodnikau [g], Sergey O. Solomevich, [g] Guohua Jiang [a,b,*]

[a] *School of Materials Science and Engineering, Zhejiang Sci-Tech University, Hangzhou, 310018, China*

[b] *International Scientific and Technological Cooperation Base of Intelligent Biomaterials and Functional Fibers of Zhejiang Province, Hangzhou, 310018, China*

[c] *College of Life Sciences and Medicine, Zhejiang Sci-Tech University, Hangzhou, Zhejiang, 310018, China*

[d] *College of Life Sciences, Xinyang Normal University, Xinyang 464000, China*

[e] *Université libre de Bruxelles (ULB), École polytechnique de Bruxelles, 3BIO10 BioMatter, Avenue F.D. Roosevelt, 50 - CP 165/61, 1050 Brussels, Belgium*

[f] *Institute of Polymer Chemistry and Physics, Uzbekistan Academy of Sciences, Tashkent, 100128, Uzbekistan*

[g] *Research Institute for Physical Chemical Problems of the Belarusian State University, Minsk, 220030, Belarus*

E-mail: katherineyfs@zstu.edu.cn (Y. Sun)

ghjiang_cn@zstu.edu.cn (G. Jiang)

Abstract: Nanoformulations for combining chemotherapy, chemodynamic therapy, and photothermal therapy have enormous potential in tumor treatment. Coating nanoformulations with cell membranes endows them with homologous cellular mimicry, enabling nanoformulations to acquire new functions and properties, including homologous targeting and long circulation *in vivo*, and can enhance internalization by homologous cancer cells. Herein, we fused multifunctional biomimetic nanoformulations based on Cu-doped zeolitic imidazolate framework-8 (ZIF-8). Hydroxycamptothecin (HCPT), a clinical anti-tumor drug, was encapsulated into ZIF-8, which was subsequently coated with polydopamine (PDA) and red blood cell membrane. The as-fabricated biomimetic nanoformulations showed an enhanced cell uptake *in vitro* and the potential to prolong blood circulation *in vivo*, producing effective synergistic chemotherapy, chemodynamic therapy, and photothermal therapy under the 808 nm laser irradiation. Together, the biomimetic nanoformulations showed a prolonged blood circulation and evasion of immune recognition *in vivo* to provide a bio-inspired strategy which may have the potential for the multi-synergistic therapy of breast cancer.

Keywords: biomimetic nanoformulations, ZIF-8, synergistic therapy, photothermal therapy, chemotherapy, erythrocyte membrane

1. Introduction

Breast cancer has emerged as a profoundly pernicious malignancy among women in contemporary times. [1] Conventional therapeutic methods such as surgical resection, chemotherapy (CT), and radiation therapy (RT) may lead to substantial challenges, [2] including elevated rates of tumor recurrence, impairment of normal cellular function, and the emergence of multidrug resistance, which make breast cancer patients endure significant and far-reaching adverse effects. [3,4] Therefore, to overcome the limitations of traditional therapies and improve breast cancer treatment, it is crucial to develop a novel nanomedicine delivery platform that enables the synergistic combination of multiple treatment modalities. [5,6] Fortunately, significant advances in nanotechnology have opened up new possibilities for the development of cancer therapies. [7]

Among these emerging nanotechnology-based therapeutic strategies, chemodynamic therapy (CDT) has attracted considerable attention due to its minimal side effects and tumor-specificity. [8,9] As a reactive oxygen species (ROS)-mediated reaction, CDT can facilitate the production of hydroxyl radicals from endogenous hydrogen peroxide through Fenton or Fenton-like reactions in the presence of metal ion catalysts (such as Fe, Cu, Mn, etc.), without relying on external light sources or stimuli. [10-12] Moreover, photothermal therapy (PTT) represents remarkable therapeutic potential as an innovative method for treating tumors. [13-15] This localized thermotherapy induces cancer cell death and promotes the ablation of tumor tissue, while concurrently minimizing any potential damage to adjacent healthy tissue.

[16-18] Significantly, the local heat generated by the photothermal effect is beneficial to increase the permeability of tumor blood vessels and tumor cell membranes, [19,20] which can facilitate the absorption and accumulation of nanoparticles, ultimately augmenting multiple treatment modalities. Therefore, the combination of conventional chemotherapy with CDT/PTT therapy not only integrates the advantages of diverse treatment modalities to optimize the synergistic anti-tumor effect, but also mitigates the side effects. [21-23] This approach presents a promising strategy to improve therapeutic efficacy in tumor treatment.

However, the Fenton-like reaction catalyzed by Cu^{+} in CDT therapies exhibits superior kinetic and energetic properties compared to Fe^{2+} due to the low redox potential of Cu^{2+}/Cu^{+} (~0.16 V), [24-26] which can facilitate the efficient oxidation of Cu^{+} to Cu^{2+} in the weakly acidic tumor microenvironment. Simultaneously, due to the inherent toxicity of free metal ions to normal cells, [27] it is essential to explore materials with controlled release capabilities for incorporating metal ions, which can minimize damage to normal cells and enhance the efficacy of tumor treatment.

Metal organic framework materials (MOFs) have attracted significant attention from researchers due to their high porosity, large specific surface area, tunable pore size and biodegradability. [28-30] Among them, zeolitic imidazolate framework-8 (ZIF-8), represents a typical class of MOF materials, exhibiting excellent biocompatibility and pH-responsive biodegradation, presenting considerable prospects for application in the biomedical field. [31-33] However, due to the inadequate photothermal properties of the MOF, it is unable to efficiently kill cancer

cells within a short period of time, and the reactive oxygen produced is insufficient for their eradication. Polydopamine (PDA) is a naturally occurring derivative of melanin in the human body that exerts excellent photothermal conversion efficiency. This phenomenon is attributed to the substantial presence of π electrons within PDA's molecular structure, [34-36] and it can also be used to improve materials' photocatalytic properties through the fast charge carriers transportation. With these in mind, we hypothesise that modification of MOFs using PDA could enhance the photocatalytic activity and photothermal effect. This enhancement would be achieved through the acceleration of photogenerated electron transfer and heightened light absorption.

However, the challenge of potential immune recognition that numerous nanoparticles encounter during delivery processes necessitates frequent surface modifications to prolong blood circulation time and improve drug accumulation at tumor sites. [37,38] Recently, the cell membrane-coated nanoparticles (CMNPs) technology has been widely applied as a novel camouflage and modification strategy in cancer therapy. [39-41] Among them, erythrocyte membranes extracted from erythrocytes are often applied to wrap the outer surface of nanoparticles due to their excellent immune evasion abilities [42,43] and prolonged blood circulation half-life characteristics, [44,45] which can effectively accumulate in tumor tissues through enhanced permeability and retention (EPR) effects, [46] providing a new way to achieve efficient drug utilization.

Herein, a multifunctional biomimetic composite nanomedicine based on metal-

organic frameworks was designed for efficient synergistic CDT/CT/PTT therapy for the treatment of breast cancer. Briefly, Cu/ZIF-8 nanoparticles prepared by the ion-doping method could achieve a controlled release of copper ions in the tumor microenvironment to trigger effective CDT therapy without causing damage to normal cells due to the inherited pH-sensitive properties of ZIF-8 nanoparticles. A clinical anti-tumor drug, 10-hydroxycamptothecin (HCPT), was selected for loading into Cu/ZIF-8 to achieve combined CDT/CT therapy. To endow the composite nanoformulations (HCPT@Cu/ZIF) with excellent photothermal performance, a polydopamine (PDA) coating layer was introduced on the surface of HCPT@Cu/ZIF to form HCPT@Cu/ZIF@PDA composite nanoformulations. They could trigger PTT with the aid of near-infrared light irradiation, which simultaneously could facilitate the CDT therapy effect and promote effective drug release as well. Finally, the HCPT@Cu/ZIF@PDA composite nanoformulations would be camouflaged by wrapping of red blood cell membrane to achieve an enhanced EPR effect while improving immune evasion ability and prolonging blood circulation to promote aggregation at tumor sites.

2. Materials and methods

2.1 Materials

Zinc nitrate hexahydrate ($Zn(NO_3)_2 \cdot 6H_2O$), cupric nitrate trihydrate ($Cu(NO_3)_2 \cdot 3H_2O$), 2-methylimidazole ($C_4H_6N_2$, 2-MIM), 10-hydroxycamptothecin (HCPT) and dopamine hydrochloride (DA·HCl) were purchased from Aladdin Bio-Chem Technology Co., Ltd (Shanghai, China). 2,7 dichlorodihydrofluorescein

diacetate (DCFH-DA), calcein-AM/PI double stain kit, 4',6-diamidino-2-phenylindole (DAPI), 3-(4,5-dimethyl-thiazol-2-yl)-2,5-diphenyl-tetrazolium bromide (MTT), and JC-1 were purchased from Beyotime Biotechnology Co., Ltd (Shanghai, China). Methylene blue (MB), hydrogen peroxide (H_2O_2, 30%) and N, N-dimethylformamide (DMF) were obtained from Sinopharm Chemical Reagent (Shanghai, China).

2.2 Characterizations

The morphology and size of the nanoformulations were observed by transmission electron microscopy (JEM-2100, Japan Electronics Corporation) and scanning electron microscopy (Ultra 55 FE-SEM, Carl Zeiss SMT, Germany). The zeta potential and hydrodynamic size of the nanoformulations were measured by a Zetasizer (Zetasizer Nano ZS, Malvern, UK). The specific surface area and pore volume were tested by a Brunauer-Emmett-Teller analyser (3H-2000PS1, Bayside Instrument Technology Co. Ltd.). The typical peak of ·OH was evaluated by electron spin resonance (A300, Bruker, Germany).

2.3 Synthesis of Cu/ZIF-8 nanoparticles

Cu/ZIF-8 nanoparticles were prepared according to the previous methods with slight modifications. [47,48] Briefly, 222.8 mg of $Zn(NO_3)_2 \cdot 6H_2O$ and 60.5 mg of $Cu(NO_3)_2 \cdot 3H_2O$ were dissolved in 10 mL methanol, stirring for 10 min. Then, 656.8 mg of 2-methylimidazole was dissolved in 30 mL methanol. Under stirring, the mixed solution was added to the 2-MIM solution. After stirring for 2 h at room temperature, the Cu/ZIF nanoparticles (CuZ) were collected by centrifugation (8000 r/min, 10 min), washed three times with methanol, and finally stored in methanol at 4 °C for further

use.

2.4 Synthesis of HCPT@Cu/ZIF nanoformulations

To obtain HCPT@Cu/ZIF nanoformulations (HCuZ), 10 mg of Cu/ZIF nanoparticles were dispersed in HCPT DMF solution (1 mg/mL) and stirred for 24 h at room temperature. After centrifugation, the HCuZ nanoformulations were collected.

2.5 Synthesis of HCPT@Cu/ZIF@PDA nanoformulations

50 mg of HCuZ nanoformulations were re-dispersed in 25 mL of Tris-HCl buffer solution (pH = 8.5, 10 mM), and 25 mg of DA·HCl was added. After stirring for 2 h, the HCPT@Cu/ZIF@PDA nanoformulations (HCuZP) were obtained by centrifugation and repeatedly washed with water to remove unreacted dopamine. Additionally, Cu/ZIF@PDA nanoformulations (CuZP) were prepared by the same procedure described above except for the absence of HCPT.

2.6 Extraction of red cell membrane

The preparation of red cell membrane was mainly performed by the previous methods. [49-51] First, whole blood was transferred into a centrifuge tube, and then, 1× PBS was added and centrifuged at 4 °C for 5 min. After washing with 1× PBS three times, red blood cells were obtained. Second, the resulting precipitate was re-dispersed in 0.25× PBS and incubated for 1 h at 4 °C in a shaker. Subsequently, the solution was centrifuged at 10,000 rpm for 5 min at 4 °C and repeatedly washed with 1 × PBS until the centrifuged supernatant turned colorless. Finally, the red cell membranes were collected and stored at -80 °C for future use.

2.7 Synthesis of RBCM-HCPT@Cu/ZIF@PDA nanoformulations

The red cell membrane-coated HCPT@Cu/ZIF@PDA nanoformulations (Rm-HCuZP) were prepared according to the reported methods. [29,52,53] In brief, 1 mL of red cell membranes (1mg/mL) was mixed with 1 mL of HCPT@Cu/ZIF@PDA (1 mg/mL) and stirred under an ice bath for 30 min, followed by sonication for 5 min, and then the mixture was extruded several times through an Avanti mini extruder (LF-1, Ottawa, Canada) using a 400 nm porous polycarbonate membrane. After removing the excess red cell membrane by centrifugation, Rm-HCuZP was eventually obtained.

2.8 Drug loading and release *in vitro*

The loading (*LE%*) and encapsulation efficiency (*EE%*) of HCPT were determined by the following formula:

$$LE\% = \frac{w_1 - w_0}{w_1} \times 100\% \quad (1)$$

$$EE\% = \frac{w_1 - w_0}{w_2} \times 100\% \quad (2)$$

where w_0 is the weight of unloaded HCPT in the supernatant, w_1 is the overall weight of HCPT, and w_2 is the weight of HCuZ.

To evaluate the drug release of Rm-HCuZP under different conditions, 30 mg Rm-HCuZP were dispersed in PBS solutions (pH 7.4 or 5.6) and transferred into dialysis bag. Then, it was immersed in PBS solution (60 mL) with or without laser irradiation (808 nm, 1 W/cm^2, 5 min). At designated time intervals, 3 mL of the sample was removed. Then, an equal amount of PBS was added. The amount of released HCPT was measured by a UV-vis spectrophotometer.

2.9 Photothermal performance

To evaluate the photothermal performance of Rm-HCuZP, 1 mL of Rm-HCuZP suspension at different concentrations (25, 50, 100, 200, and 400 μg/mL) was transferred into a 1.5 mL Eppendorf tube and exposed to laser irradiation (808 nm, 1 W/cm^2) for 10 min. An aqueous solution was adopted as a control. Meanwhile, the temperature of these solutions was measured every 10 s with the aid of an infrared thermal imager. Additionally, the solution temperature of Rm-HCuZP at a concentration of 400 μg/mL was monitored by the same method at different laser irradiation powers (0.4, 0.6, 0.8, and 1.0 W/cm^2). To investigate the photothermal stability of the Rm-HCuZP, the solution (400 μg/mL) was irradiated at 1 W/cm^2 in four repetitive cycles of 5 min on and 5 min off, and the temperature variations were recorded in the same way as described above.

2.10 ·OH generation measurement

The ·OH generated by Rm-HCuZP through Fenton-like reaction was detected using MB and ESR methods. [54,55] For the detection of MB, the Rm-HCuZP at different concentrations (0, 25, 50, 100, and 200 μg/mL) were incubated with methylene blue (MB) solution (10 μg/mL) and H_2O_2 (1 mM) in PBS buffer (pH = 5.6) for 15 min. The absorbance spectrum of the mixture was measured using a UV-vis spectrophotometer, with MB solution as the blank control. In addition, the fixed concentration of Rm-HCuZP solution was 50 μg/mL, and it was incubated with MB solution (10 μg/mL) and H_2O_2 (1 mM) in PBS buffer (pH = 7.4, pH = 5.6, and pH = 5.6 + laser) for 15 min. The absorbance spectrum was then measured using a UV-vis spectrophotometer. ESR measurements were performed by coincubating Rm-HCuZP

(pH = 7.4, pH = 5.6 and pH = 5.6 + laser) with H_2O_2 (1 mM) and DMPO, followed by detection of the presence of ·OH production by ESR.

2.11 *In vitro* hemolysis assay

The hemolytic toxicity of nanoformulations *in vitro* was assessed by employing mouse blood. [56] Specifically, 500 μL of fresh mouse blood was placed in a centrifuge tube and the supernatant was discarded after centrifugation at 3,500 rpm for 5 min. Then, the bottom sediment was washed three times with PBS and eventually diluted with PBS to obtain a 1% (v/v) erythrocyte suspension. Then, 200 μL of the above solution was added to 800 μL of Rm-HCuZP dispersion to formulate solutions of different concentrations (400, 200, 100, 50 and 25 μg/mL). After incubation at 37 °C for 12 h, the supernatant was extracted by centrifugation and the absorbance value at 540 nm was monitored by a UV-vis spectrophotometer. PBS and deionized water were included as negative and positive control groups, respectively. The hemolysis rate was calculated by the following formula:

$$Hemolysis\ ratio(\%) = \frac{A_{sample} - A_{negative}}{A_{positive} - A_{negative}} \times 100\% \quad (3)$$

2.12 Cytotoxicity study

The MTT assay was applied to estimate the relative cell viability of various materials. The 4T1 cells were seeded at a cell density of 1×10^5/well in 96-well plates with DMEM medium containing 10% fetal bovine serum and 1% double antibodies (penicillin-streptomycin solution), and then incubated in a constant temperature (37°C) incubator with 5% CO_2 for 24 h to allow the cells to grow against the wall. Afterwards, the initial medium was replaced by fresh DMEM medium containing

different concentrations of CuZP, CuZP+NIR, HCuZP, HCuZP+NIR, Rm-HCuZP, and Rm-HCuZP+NIR (0, 5, 10, 20, 30, 40, and 50 μg/mL), respectively. For the laser irradiation group, after 4 h of incubation, cells were treated with an 808 nm laser at a power density of 1 W/cm^2 for 5 min and then incubated for an additional 20 h before application of MTT reagent. After 24 h of incubation, 20 μL of MTT solution (5 mg/mL) was added after washing with PBS and further incubated for 4 h. Finally, 150 μL of DMSO solution was added to each well, and cell viability was calculated by measuring the absorbance at 490 nm.

The 4T1 cells were inoculated in confocal culture dishes at a cell density of 1 × 10^5/well, and the medium was changed to fresh medium containing CuZP, HCuZP and Rm-HCuZP (50 μg/mL) after overnight incubation. For the laser irradiation group, the cells were exposed to an 808 nm laser (1 W/cm^2, 5 min) after 4 h of incubation. Then after another 20 h incubation, 4T1 cells were stained with Calcein-AM and propidium iodide (PI) for 15 min under dark conditions. In the end, the cells were visualized with the aid of laser confocal microscopy (CLSM) after washing with PBS three times.

2.13 *In vitro* mitochondrial membrane potential

The 4T1 cells were inoculated in confocal culture dishes overnight. The cells were treated with PBS, PBS+NIR, CuZP, CuZP+NIR, HCuZP, HCuZP+NIR, Rm-HCuZP, and Rm-HCuZP+NIR for 6 h. For the laser irradiation group, the cells were exposed to an 808 nm laser (1 W/cm^2, 5 min) after 4 h of incubation. Finally, the cells were stained by a mitochondrial membrane potential assay kit with JC-1.

2.14 *In vitro* cellular uptake

The uptake ability of various materials by 4T1 cells was evaluated using laser confocal microscopy (CLSM). Specifically, HCuZP and Rm-HCuZP labelled with FITC were prepared to assess the internalization ability. Then, 4T1 cells were seeded at a density of 1×10^5 cells/well in confocal dishes. After 12 h of incubation, the culture medium was replaced with fresh medium containing HCuZP, Rm-HCuZP, and FITC (50 μg/mL), with PBS as the control. After another 4 h of incubation, the remaining materials were washed away with PBS three times, followed by fixation with 4% paraformaldehyde for 15 min and DAPI staining for 20 min. The fluorescent images were acquired by CLSM. The cellular uptakes of HCuZP and Rm-HCuZP by RAW264.7 cells were assessed to explore the ability of immune escape.

2.15 *In vitro* •OH generation

The levels of ROS induced by Rm-HCuZP in different conditions were detected by CLSM and flow cytometry using ROS probe (DCFH-DA). The 4T1 cells were first seeded in confocal culture dishes at a cell density of 1×10^5/well. Then, the previous medium was discarded after 12 h of incubation, and the cells were treated with PBS, H_2O_2, Rm-HCuZP, Rm-HCuZP+H_2O_2, and Rm-HCuZP+H_2O_2+NIR for 6 h. For the laser irradiation group, the cells were exposed to an 808 nm laser (1 W/cm^2, 5 min) after 4 h of incubation. After washing with PBS to remove the residual material, the fluorescent probe DCFH-DA was added and cocultured for 20 min. Finally, fluorescent images of DCFH were captured by CLSM to evaluate the ROS level of the prepared material. The flow cytometry was used to quantitatively detect the

connection between the concentration Rm-HCuZP and production of intracellular ROS.

2.16 Tumor model of breast cancer

Balb/c female mice (4-5 weeks old, 20 ± 2 g) were provided by Zhejiang Hangzhou Hock Biotechnology Co. To establish tumor models, 50 μL of 5×10^5 4T1 cancer cells were injected subcutaneously in saline into the right inguinal location of mice. All experiments were approved and conducted under the guidance of the Experimental Animal Welfare Ethics Committee of the Zhejiang Experimental Animal Center (animal approval number: ZJCLA-IACUC-20010255) and the Animal Ethics Committee of Zhejiang Sci-Tech University (animal approval number: 20230314011).

2.17 *In vivo* fluorescence and photothermal properties

The *in vivo* fluorescence images were used to investigate the distribution of Rm-HCuZP. Firstly, the FITC-labelled CuZP, HCuZP, and Rm-HCuZP solution (200 μL, 15 mg/kg) were injected intravenously into the mice through the tail. And then, the fluorescence images were recorded at 2, 6, 12, 24, and 48 h after drug administration. For photothermal images, PBS, CuZP, HCuZP and Rm-HCuZP (200 μL, 15 mg/kg) were injected through the tail vein, respectively. After 12 h of treatment, each group was irradiated with an 808 nm laser (1 W/cm^2) for 10 min, while the thermograph images of the tumor-bearing mice were recorded by infrared thermography.

2.18 *In vivo* anti-tumor therapy evaluation

After the tumor volume reached 50-100 mm^3, the tumor-bearing mice were randomly separated into 8 groups (n=5): (i) PBS group (without any treatment); (ii)

PBS+NIR group (treated by NIR irradiation only); (iii) CuZP group (treated by CuZP only); (iv) CuZP+NIR group (treated by CuZP and NIR irradiation); (v) HCuZP group (treated by HCuZP only); (vi) HCuZP+NIR group (treated by HCuZPand NIR irradiation); (vii) Rm-HCuZP group (treated by Rm-HCuZP only); and (viii) Rm-HCuZP+NIR group (treated by Rm-HCuZP and NIR irradiation). All groups were intravenously injected via the tail vein every 2 days. Then for the laser groups, the 808 nm laser (1 W/cm^2, 10 min) was utilized in the irradiation treatment at 12 h post-injection. During the treatment, the body weight and tumor volume of all mice were recorded every two days, and the tumor volume was calculated according to the formula: volume = length × (width)^2/2.

After 12 days of treatment, all mice were sacrificed by cervical dislocation and dissected to obtain the tumors as well as the vital organs, including the heart, liver, spleen, lung and kidney. Then, all excised tumors were weighed and recorded. Subsequently, the isolated tumors and major organs of each group were randomly selected for histological and immunohistochemical analysis (H&E, TUNEL, and Ki67), by 4% paraformaldehyde fixation, embedding, and staining, as a comprehensive assessment of the tumor suppression effect of different treatment modalities.

2.19 Statistical Analysis

Statistical analysis was conducted via GraphPad Prism 8 and Origin software. Data were analysed with ordinary one-way ANOVA by Tukey's means comparison method. *$p < 0.05$, **$p < 0.01$, ***$p < 0.005$, ****$p < 0.0001$. Data are expressed as

the means ± SDs. A value of $p < 0.05$ was considered statistically significant.

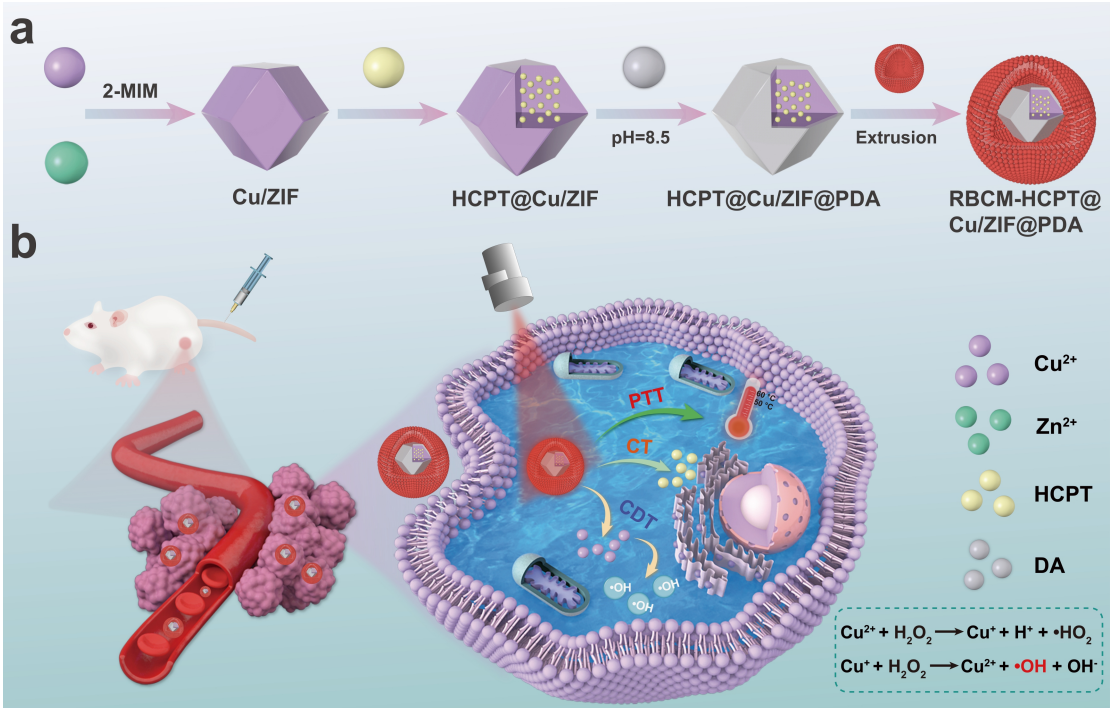

Scheme 1. (a) Schematic design of Rm-HCuZP NFs; (b) Therapeutic mechanism of Rm-HCuZP NFs for efficient synergistic cancer therapy.

3. RESULTS AND DISCUSSION

3.1 Preparation and characterization of Rm-HCuZP nanoformulations

The preparation procedure of red blood cell membrane-coated functionalized Cu-doped metal organic framework nanoformulations (Rm-HCuZP) is shown in Scheme 1a. Firstly, Cu-doped ZIF-8 nanoparticles (CuZ) were synthesized by an ion-doping strategy using a modified method. [47,48] These CuZ nanoparticles have a rhombic dodecahedral structure with an average diameter of ~100 nm that is confirmed by TEM (Figure 1a) and SEM (Figure S1) measurements. Figure 1e shows the X-ray powder diffraction (XRD) patterns of ZIF-8-based derivatives. Almost no significant difference can be found between Cu-doped ZIF-8 and pure ZIF-8, indicating that the doping of copper ions does not influence the crystal structure of

ZIF-8. The energy-dispersive X-ray spectroscopy (EDS) results demonstrate the ratio of the C, N, O, Zn, and Cu atomic contents (Figure S2). In addition, the elemental mapping of CuZ exhibits the uniform distribution of C, N, O, Zn, and Cu elements within the nanostructure (Figure 1f). The surface elemental composition of CuZ was investigated using X-ray photoelectron spectroscopy (XPS). The full spectrum XPS measurement of CuZ reveals peaks corresponding to C 1s, N 1s, O 1s, Zn 2p, and Cu 2p (Figure 1g and S3), confirming the successful incorporation of Cu ions into ZIF-8.

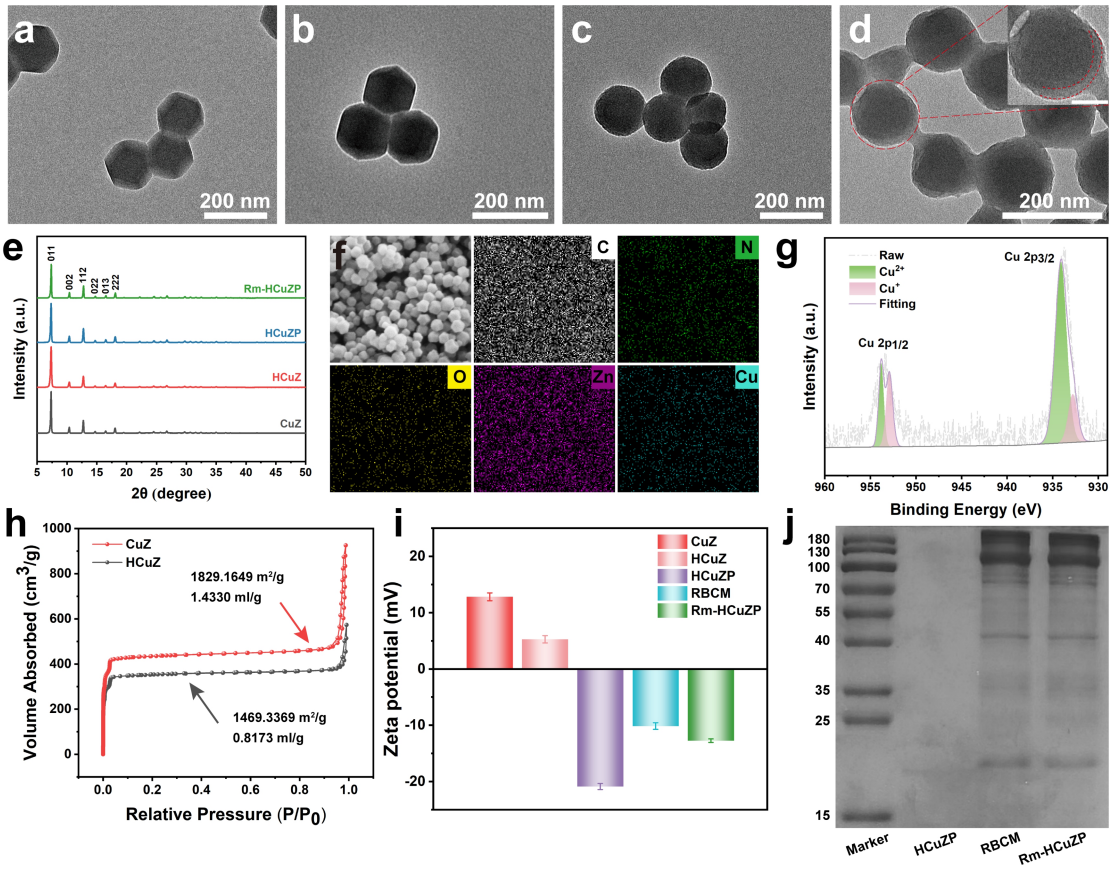

Figure 1. TEM images of (a) CuZ, (b) HCuZ, (c) HCuZP, and (d) Rm-HCuZP. Scale bar: 200 nm (insert scale bar: 50 nm). (e) X-ray powder diffraction analysis of CuZ, HCuZ, HCuZP, and Rm-HCuZP. (f) Elemental mapping of C, N, O, Zn, and Cu in CuZ. (g) XPS high resolution spectrum of Cu 2p in CuZ. (h) Nitrogen adsorption-desorption isothermal curve of CuZ and HCuZ. (i) Zeta potential of CuZ, HCuZ, HCuZP, and Rm-HCuZP. (j) SDS-PAGE protein analysis of Rm, HCuZP, and Rm-HCuZP.

Subsequently, HCPT and CuZ were stirred in DMF solution for 24 h to obtain HCPT-loading composite nanoformulations (HCuZ) due to the higher porosity and larger specific surface area of CuZ (Figure 1h). And the drug loading was calculated to be 19.1% by UV-vis absorption spectra (Figures S4 and S5). The morphology of the resultant HCuZ is close to the CuZ (Figure 1b). Afterwards, a polydopamine (PDA) shell layer is coated on the surface of HCuZ (HCuZP) via the self-polymerization of dopamine under weakly alkaline and aerobic conditions to avoid the rapid release of loaded drugs. Meanwhile, the surface of HCuZP becomes rough, as shown in Figure 1c. Finally, red blood cell membrane-coated functionalized Cu-doped metal organic framework nanoformulations (Rm-HCuZP) are prepared by co-extruding red blood cell membrane (Rm) and HCuZP nanoformulations using a liposome extruder. Figure 1d shows the TEM image of Rm-HCuZP with size ~160 nm in diameter, exhibiting a uniform layer of red blood cell membrane on the surface of particles and a certain degree of adhesion between particles, which may mainly due to the electrostatic adsorption between the nanoparticles and the cell membranes. [57] To determine the encapsulation of Rm on the surface of nanoformulations, the surface charge of nanoformulations was investigated by the zeta potential. As shown in Figure 1i, the CuZ possess a positive charge (~12 mV) which can adsorb HCPT anions due to their Lewis acidic surface. And the potential changed from positive (~5 mV) to negative (-20 mV) after coating with PDA due to the presence of PDA hydroxy groups. After encapsulating the outermost layer of the red cell membrane, the potential of Rm-HCuZP increased to -12 mV, which is close to that of the red blood

cell membrane itself (-10 mV). Additionally, the hydrodynamic sizes of CuZ (~100 nm), HCuZ (~129.9 nm), HCuZP (~141.3 nm) and Rm-HCuZP (~160.1 nm) can further demonstrate the successful preparation of nanoformulations (Figure S6). To investigate the stability of Rm-HCuZP, the particle size, polydispersity index (PDI) and zeta potentialthey were tested after dispersion of them in PBS for one week. As shown in Figure S7, the changes of particle size and polydispersity index (PDI) are negligible, and the zeta potential exhibits no significant difference. Moreover, the presence of Rm on the surface of nanoformulations was further verified by the sodium dodecyl sulfate-polyacrylamide gel electrophoresis (SDS-PAGE). The protein bands of Rm and Rm-HCuZP are identical (Figure 1j), which is a crucial characteristic while performing their desired functions in this study. Specially, it is expected that Rm-HCuZP will be endowed with the benefits of red blood cell membranes, which can make Rm-HCuZP invisible to evade immune recognition.

3.2 TME-responsive biodegradation performance and drug release behavior

To validate the sensitive pH-responsive biodegradation properties of CuZ nanoparticles, they were dispersed in PBS with different pH values (pH = 7.4 mimicking the normal human tissue environment, and pH = 5.6 simulating the tumor microenvironment). [58-62] The solutions were collected at 1, 6, 12, and 24 h to observe their morphology change by TEM. As shown in Figure 2a, the structure of CuZ nanoparticles remains intact at pH = 7.4, indicating that they have not been destroyed under a mild environment. Under pH = 5.6 condition, CuZ nanoparticles' structure gradually disintegrates over time and eventually completely disappears after

soaking for 24 h, which can be attributed to the sensitive pH-responsive biodegradation of CuZ nanoparticles. These findings suggest that CuZ nanoparticles might potentially maintain stability within normal tissues and exhibit responsiveness to release in the acidic tumor microenvironment, which could make them a promising candidate as a biodegradable carrier.

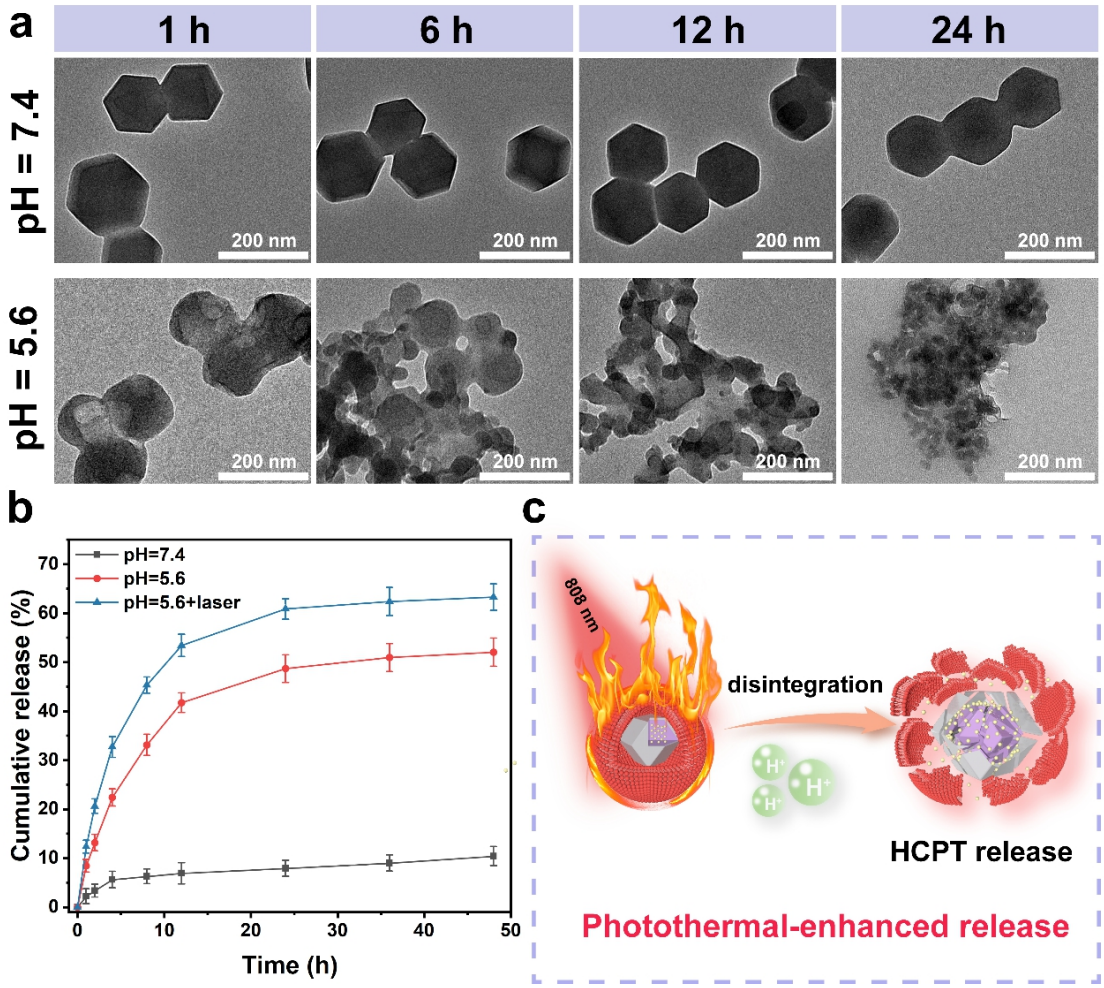

Figure 2. (a) TEM images of CuZ nanoparticles dispersed in buffer solutions of pH 7.4 and 5.6 at different time intervals, Scale bar: 200 nm. (b) Release of HCPT from Rm-HCuZP under different conditions. (c) Schematic illustration of HCPT release from Rm-HCuZP upon 808 nm laser irradiation in the acidic environment.

Furthermore, CuZ nanoparticles were used as carriers for the loading of the model drug HCPT, which was then encapsulated with PDA coatings and red cell

membranes to enhance the anti-tumor effect of the Rm-HCuZP nanoformulations. Subsequently, the drug release behaviors of the as-fabricated Rm-HCuZP nanoformulations under different conditions was initially evaluated to examine the degradability of them. As shown in Figure 2b, the drug release rate in Rm-HCuZP is approximately 10% at pH = 7.4 for 48 h, indicating that Rm-HCuZP can prevent the leakage of the drug, thus facilitating the reduction of drug side effects and achieving safe and effective drug delivery. However, the release rate of Rm-HCuZP can be increased to ~51% at pH = 5.6, which is probably attributed to the acid-responsive property of Rm-HCuZP, allowing gradual degradation and drug release in an acidic environment. Importantly, after 808 nm laser irradiation, the release rate can be further enhanced to ~63% at pH = 5.6, which is higher than that of without laser irradiation. It can be contributed to the photocatalysis of drug carriers to destroy red cell membranes and PDA coatings, leading to promote drug release. These results indicate that Rm-HCuZP possesses the pH-dependent and NIR-responsive release properties (Figure 2c).

3.3 ROS generation of Rm-HCuZP nanoformulations

Since methylene blue (MB) can change its color from blue to colorless by reacting with ·OH, accompanied by a decrease in the characteristic absorption peak at 665 nm. [63] Therefore, it can be employed to assess the catalytic activity of Rm-HCuZP in generating ·OH from H_2O_2. As shown in Figure 3a, the addition of H_2O_2 (1 mM) to the MB does not result in a significant change in the absorbance value at 665 nm, indicating the absence of a catalytic effect of H_2O_2 on MB. Moreover, incubating

the MB aqueous solution with Rm-HCuZP (25, 50, 100, and 200 μg/mL) for 15 min, the mixed solution exhibits a concentration-dependent decrease of characteristic absorption peak, suggesting that the doped copper ions can generate ·OH through a Fenton-like reaction with H_2O_2 and result in the degradation of MB.

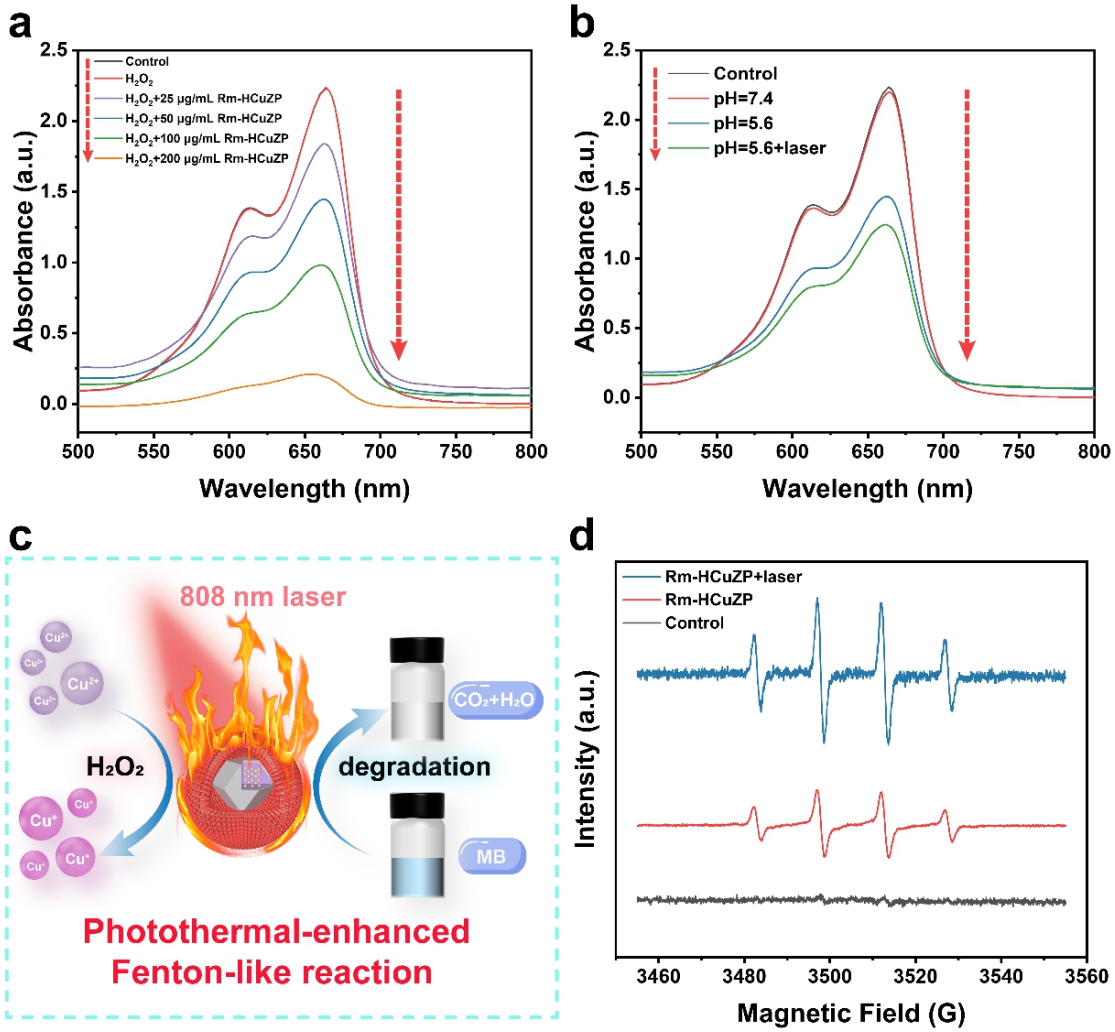

Figure 3. (a) UV-visible spectra of MB aqueous solution with H_2O_2 after the addition of different concentrations of Rm-HCuZP (25, 50, 100, and 200 ug/mL). (b) UV-visible spectra of MB aqueous solution added with Rm-HCuZP (50 ug/mL) under different conditions. (c) Schematic illustration of MB detection of ·OH from Rm-HCuZP. (d) ESR spectra of ·OH trapped by DMPO for Rm-HCuZP (200 ug/mL) under different treatments at pH = 5.6.

As illustrated in Figure 3b, the degradation effect of Rm-HCuZP on MB in an acidic environment (pH = 5.6) is more significant compared to a neutral environment

(pH = 7.4), which is attributed to the sensitive pH-responsive capacity of Rm-HCuZP. This feature can be beneficial to mitigate the potential harm of free copper ions to normal cells. More importantly, the absorbance intensity of MB significantly decreases after NIR irradiation, suggesting that more ·OH are consumed, which is due to the excellent photothermal conversion of Rm-HCuZP, thus promoting the Fenton-like reaction. These results demonstrate that Rm-HCuZP can realize the effective release of copper ions at low pH and enhance the Fenton-like reaction. (Figure 3c).

In addition, the generation of ·OH is confirmed through an electron spin resonance (ESR) spectrometry using DMPO as the trapping agent. [64] As shown in Figure 3d, the distinctive 1:2:2:1 spectrum attributed to ·OH can be clearly observed after incubation with Rm-HCuZP. However, no ESR signals can be founded in the control group. Notably, the ESR intensity can be increased after NIR irradiation, further confirming the photothermal-enhanced Fenton-like reaction of Rm-HCuZP.

3.4 Photothermal properties of Rm-HCuZP nanoformulations

The photothermal conversion efficiency of the Rm-HCuZP was evaluated by measuring the temperature changes under NIR irradiation. Firstly, the Rm-HCuZP dispersions with different concentrations (50, 100, 150, 200, 400 μg/mL) were exposed to the 808 nm laser (1 W/cm^2) and irradiated for 10 min. As shown in Figures 4a and b, after irradiation, the temperature of the Rm-HCuZP solution (400 μg/mL) increased from 23 to 63.1 °C within 10 min, while no significant change (from 23 to 26.1 °C) was observed in the control aqueous solution during the same irradiation period. This observation indicates the excellent photothermal feature of Rm-HCuZP.

In addition, the photothermal feature of Rm-HCuZP shows a concentration-dependence characteristic.

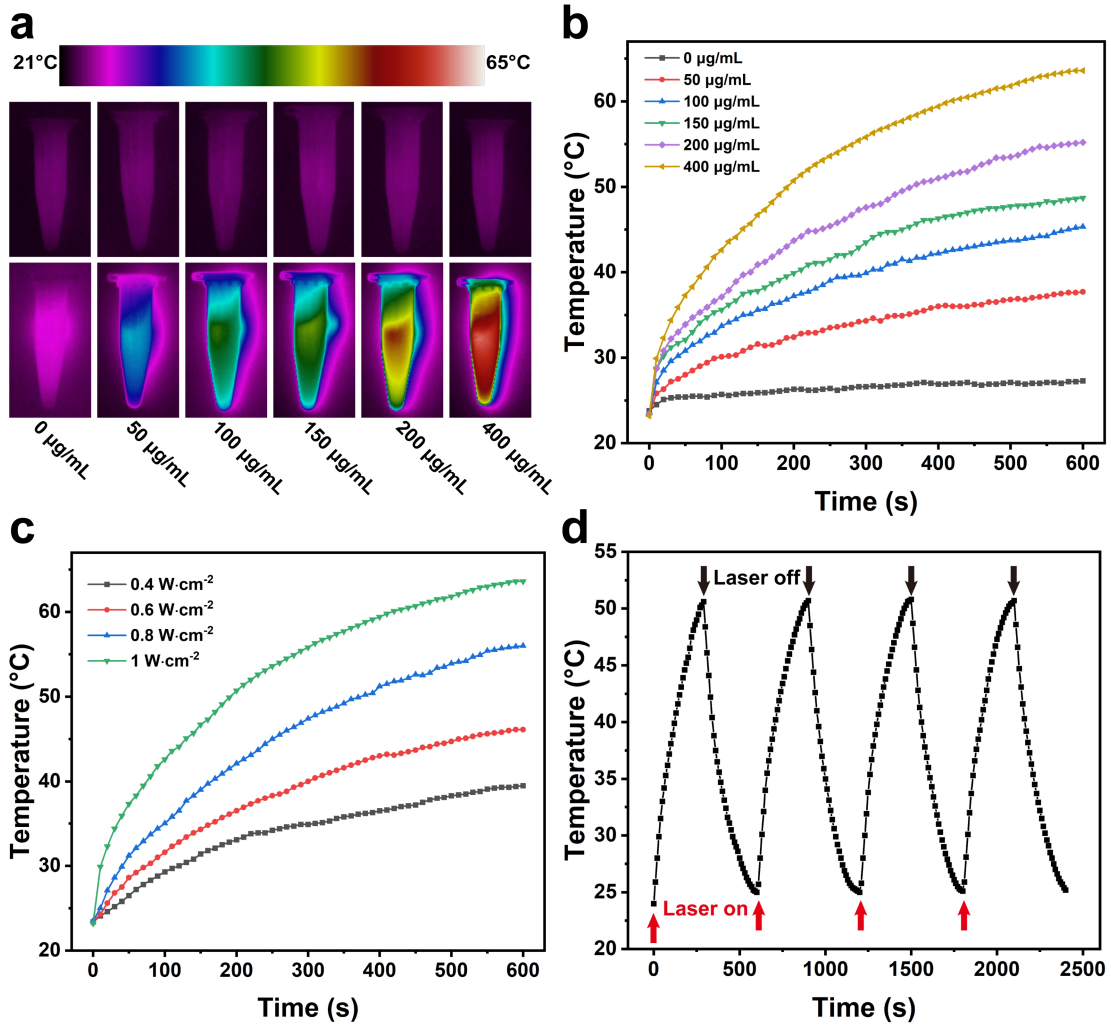

Figure 4. (a) Corresponding infrared thermal images, and (b) Temperature elevation curves of Rm-HCuZP solution with various concentrations (0, 50, 100, 150, 200, 400 μg/mL) under 808 nm laser irradiation (1 W/cm^2, 10 min). (c) Temperature change curves of the Rm-HCuZP solution (400 μg/mL) with different laser power densities (0.4, 0.6, 0.8, 1 W/cm^2). (d) Temperature change curves of the Rm-HCuZP solution (400 μg/mL) over four cycles of laser on/off under 808 nm laser irradiation (1 W/cm^2).

The temperature of Rm-HCuZP dispersions can be increased to 37.7, 45.3, 48.7, 55.2 and 63.6 °C for the concentration at 50, 100, 150, 200 and 400 μg/mL after irradiation for 10 min. Furthermore, as increasing laser power density from 0.4 to 1.0

W/cm^2, the temperature of Rm-HCuZP dispersion (400 μg/mL) shows a power-dependent relationship (Figure 4c). To further investigate the photothermal stability of Rm-HCuZP NFs, the Rm-HCuZP solution was subjected to four cycles of NIR irradiation (1 W/cm^2). As shown in Figure 4d, the temperature changes show no significant fluctuation during the four cycles, in which the maximum temperatures are on the order of 50.6, 50.7, 50.8, and 50.7 °C, demonstrating the superior photothermal stability of Rm-HCuZP.

3.5 Cytotoxicity assessment *in vitro*

To investigate the cytotoxicity of Rm-HCuZP *in vitro*, 4T1 cells were performed using a MTT method. Figure 5a shows the cell viability against CuZP, HCuZP, and Rm-HCuZP with a concentration ranging from 5 to 50 μg/mL without NIR irradiation. The survival of 4T1 cells exhibits a concentration-dependent relationship, and a signature cytostatic effect can be observed after Rm-HCuZP treatment (~40% at 50 μg/mL) compared to CuZP and HCuZP, which can be attributed to the enhanced aggregation capability of nanoformulations in tumor cells due to the presence of red cell membranes. Additionally, a reduction in cell viability is detected for all groups after NIR irradiation treatment (Figure 5b). However, the control group does not exhibit significant alteration in cell viability with NIR irradiation treatment alone, suggesting laser irradiation alone can not cause cellular damage (Figure 5c and S8). And the Rm-HCuZP+NIR group exhibits the lowest cell viability among all groups, which might be contributed to the improved cell phagocytic ability by cell membranes functionalization and the synergistic effect of CT, CDT, and PTT.

Calcein AM/PI staining was also applied to evaluate the living (green) and dead (red) cells after being treated by nanoformulations. [58] As shown in Figure 5d, the predominant green fluorescent signal can be observed in PBS and PBS+NIR groups without any treatment, indicating no signature effect for the survival of cells with NIR exposure only. A certain degree of red fluorescent signal can be revealed in 4T1 cells treated by nanoformulations, suggesting the presence of cellular damage. Among them, 4T1 cells co-cultured with Rm-HCuZP under 808 nm laser irradiation (1 W/cm^2, 10 min) exhibit the strongest red and weakest green fluorescent signals. Combining the above results, Rm-HCuZP shows the highest cytotoxicity *in vitro* against 4T1 cells with NIR irradiation. Meanwhile, the fluorescence intensity of confocal images were quantitatively analyzed by Image J. [10, 23, 65, 66] And the analysis results of Calcein-AM and PI are consistent with the above results (Figure 5e).

The mitochondrial membrane potential (MMP) of 4T1 cells was also detected by JC-1 staining (red for a normal membrane potential, and green for an impaired membrane potential). [67] As shown in Figure 5f, the control groups (PBS and PBS+NIR) produce strong red fluorescence, suggesting no damage to mitochondria. In contrast, the Rm-HCuZP+NIR group exhibits the strongest green fluorescence signal in all groups, implying the existence of more impaired mitochondria, which is consistent with the results of quantitative fluorescence analysis of the aggregates and monomers of JC-1 in 4T1 cells (Figure S9).

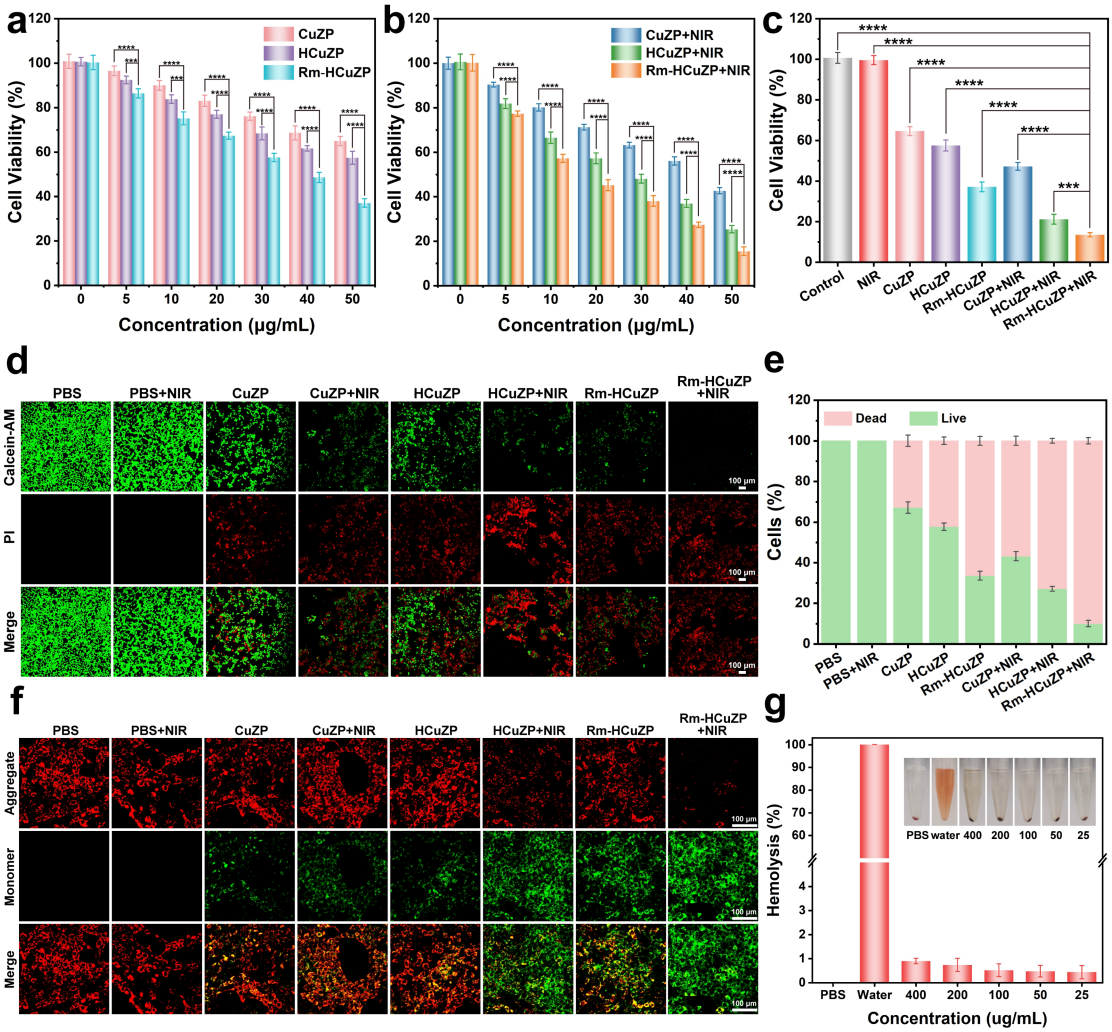

Figure 5. (a) Cell viability of 4T1 cells incubated with different concentrations (from 0 to 50 μg/mL) of CuZP, HCuZP, and Rm-HCuZP without or with (b) NIR irradiation (1 W/cm^2, 10 min). (c) Cell viability of 4T1 cells incubated with PBS, CuZP, HCuZP, and Rm-HCuZP at a concentration of 50 μg/mL with or without NIR irradiation. (d) Fluorescence images of 4T1 cells incubated with Calcein-AM and PI under different treatments (scale bar = 100 μm). (e) Quantitative analysis of fluorescence intensity based on CLSM images shown in Figure 5d via Image J. (f) The CLSM images of MMP labelled by JC-1 probe in 4T1 cells incubated with different treatments (scale bar = 100 μm). (g) Hemolysis tests and images with different concentrations (0, 25, 50, 100, 200, and 400 μg/mL) of Rm-HCuZP and H_2O. The data for comparisons are shown to be significant, where *$p < 0.05$, **$p < 0.01$, *** $p < 0.001$, and **** $p < 0.0001$.

Furthermore, hemolysis assays were conducted to evaluate the biocompatibility

of Rm-HCuZP as an intravenous drug delivery formulation prior to *in vivo* experiments. As shown in Figure 5g, the hemolysis rate of Rm-HCuZP is below 5% for all samples, with concentrations ranging from 25 to 400 μg/mL, indicating the excellent blood biocompatibility of the Rm-HCuZP.

3.6 Cellular uptake and ROS generation *in vitro*

To investigate the aggregation of Rm-HCuZP inside tumor cells, the cellular uptake of Rm-HCuZP by 4T1 cells was evaluated by CLSM. As shown in Figure 6a, after incubating 4T1 cells with fluorescence-labelled HCuZP and Rm-HCuZP for 4 h. Rm-HCuZP group exhibits a stronger green fluorescence signal which closely encircled the nucleus (blue). However, almost no fluorescence is displayed in the PBS and FITC groups, indicating no fixation of FITC. In addition, a relative weaker green fluorescence signal can be observed in HCuZP group compared with Rm-HCuZP group. This result indicates that the red blood cell membrane outside the carrier is beneficial to cellular uptake of the as-fabricated nanoformulations.

In addition, anti-phagocytosis tests were performed to evaluate the immune escape ability of Rm-HCuZP. As shown in Figure 6b and S10, after incubating RAW264.7 cells with FITC-labelled HCuZP and Rm-HCuZP, compared to the higher fluorescence intensity of the HCuZP group (without encapsulated erythrocyte membranes), the Rm-HCuZP group shows a relative weaker fluorescence intensity, suggesting that the presence of RBCM effectively reduces the phagocytosis of macrophages, [52, 68, 69] thus offering the possibility to prolong the circulation of nanoformulation *in vivo*.

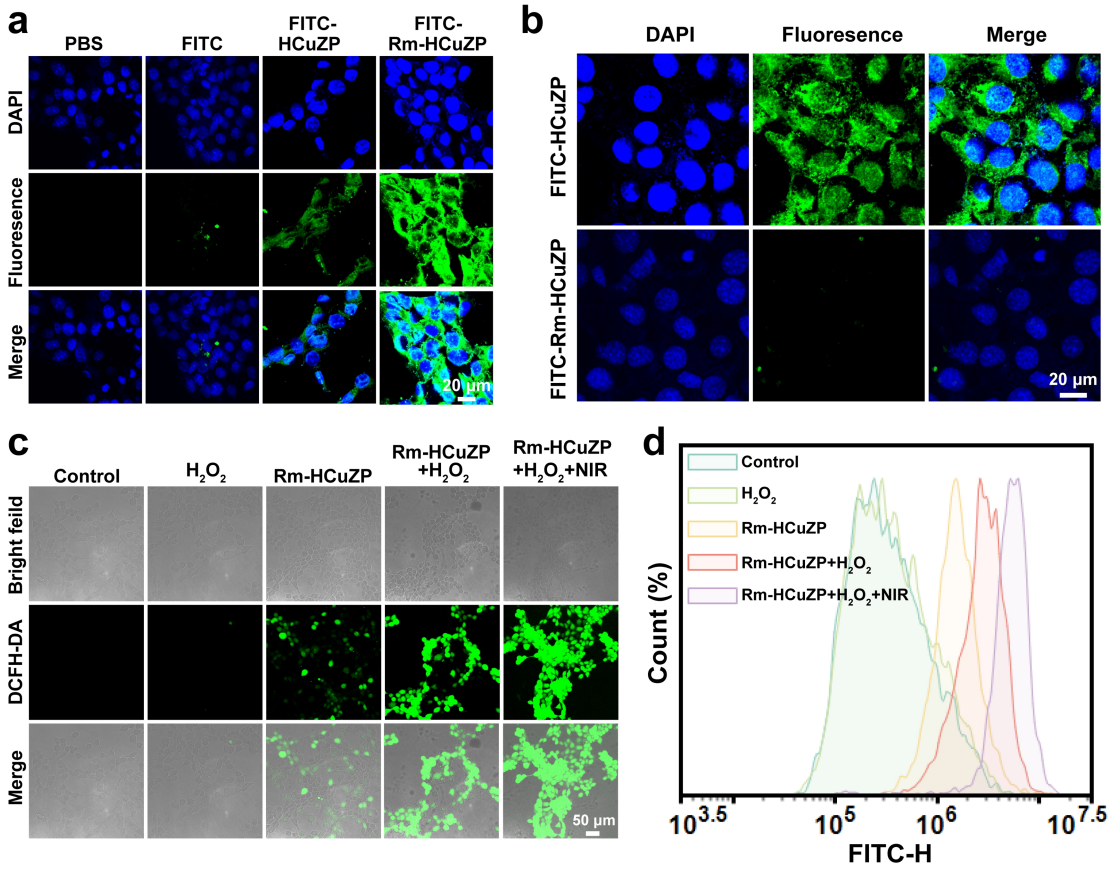

Figure 6. (a) Fluorescence images of 4T1 cells incubated with DAPI in different groups (scale bar = 10 μm). (b) CLSM images of RAW264.7 cells incubated with DAPI in different groups. (c) Fluorescence images of 4T1 cells incubated with DCFH-DA in various groups (scale bar = 50 μm). (d) Flow cytometry analysis of intracellular ROS in 4T1cells.

To evaluate the ROS generation capability of Rm-HCuZP, the expression levels of ·OH radicals in 4T1 cells after different treatments were detected using the DCFH-DA probe. [70] As shown in Figure 6c, no green fluorescence signal can be observed in the control group, and a slight fluorescence is observed in the Rm-HCuZP group. However, the fluorescence signal can be significantly enhanced by the addition of exogenous H_2O_2 into Rm-HCuZP group, indicating an obvious increase of intracellular ·OH content. After subjecting 4T1 cells to NIR irradiation for 10 min, the fluorescence intensity further improved, promoting the Fenton-like activity and elevating the intracellular ·OH radical level. The flow cytometry was further used for

qualitative analysis to further corroborate the ROS production. As shown in Figure 6d, compared with the control group, the Rm-HCuZP group exhibits a certain degree of ROS accumulation, and a stronger ROS aggregation from the Rm-HCuZP+NIR group can be detected with laser irradiation.

3.7 Biodistribution and photothermal properties *in vivo*

To investigate the distribution of Rm-HCuZP *in vivo*, FITC-labelled CuZP, HCuZP, and Rm-HCuZP were intravenously injected *via* the tail vein into tumor-bearing mice. The fluorescence image results of tumor-bearing mice at different time periods (2, 6, 12, 24, and 48 h) are shown in Figure 7a and 7b. It can be founded that the fluorescence intensity is gradually increased at the tumor site with the extended retention time. And the maximum fluorescence intensity can be detected after administration for 12 h, indicating the greatest aggregation of nanoformulations at the tumor site at 12 h post-injection. In addition, the Rm-HCuZP group exhibits the stronger fluorescence intensity in comparison with that of CuZP and HCuZP groups. More importantly, the fluorescence intensity of the CuZP group and HCuZP group are gradually decreased over time. However, a fluorescence signal still can be observed in the Rm-HCuZP group even after injection for 48 h, which suggests that the nanoformulation wrapped the red cell membranes can prolong the circulation time and improve the EPR effect, thus achieving the enrichment in the tumor site to effectively improve the therapeutic effect.

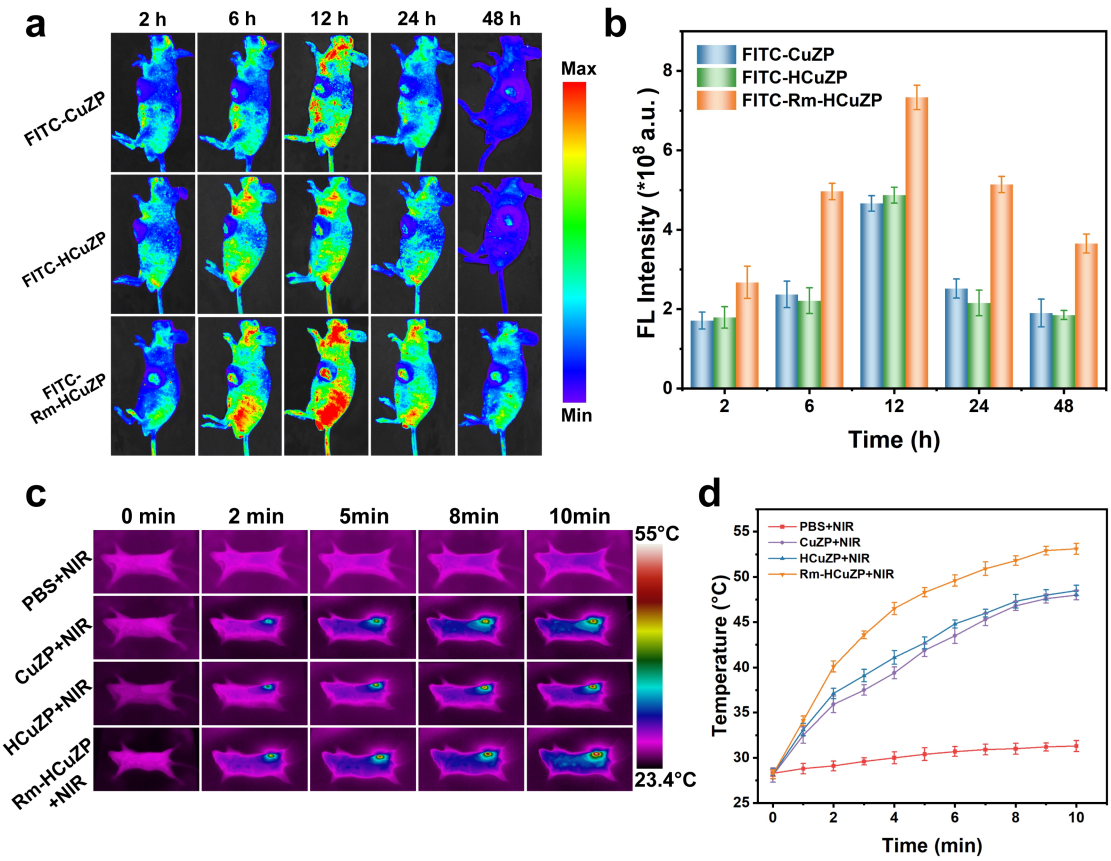

Figure 7. (a) *In vivo* fluorescence images and (b) corresponding fluorescence intensity of the tumor-bearing mice after injection with FITC-CuZP, FITC-HCuZP, and FITC-Rm-HCuZP via the tail vein at different time intervals. (c) Infrared thermal images of tumor-bearing mice and (d) corresponding tumor temperature of mice treated with PBS, CuZP, HCuZP, and Rm-HCuZP under 808 nm laser irradiation.

To evaluate the photothermal performance of Rm-HCuZP *in vivo*, CuZP, HCuZP and Rm-HCuZP were injected into mice for 12 h and then irradiated by an 808 nm laser for 10 min (1 W/cm^2). The temperature changes *in vivo* were recorded by infrared thermography. As shown in Figure 7c and 7d, no significant temperature change can be observed for the PBS group before and after irradiation. However, compared with the CuZP and HCuZP groups, the temperature at the tumor site can be significantly increased in the Rm-HCuZP group. And it can be reached 50 °C in a

short period of irradiation (10 min). These results suggest that Rm-HCuZP might possess not only notable photothermal conversion capabilities but also a potential tendency to aggregate at tumor sites, which can potentially contribute to the ablation of tumor cells.

3.8 Anti-tumor effect *in vivo*

To further evaluate anti-tumour effects *in vivo*, an animal experimental protocol was conducted, as illustrated in Figure 8a. Tumor-bearing mice were randomly divided into 8 groups: (i) PBS group (without any treatment); (ii) PBS+NIR group (treated by NIR irradiation only); (iii) CuZP group (treated by CuZP only); (iv) CuZP+NIR group (treated by CuZP and NIR irradiation); (v) HCuZP group (treated by HCuZP only); (vi) HCuZP+NIR group (treated by HCuZP and NIR irradiation); (vii) Rm-HCuZP group (treated by Rm-HCuZP only); and (viii) Rm-HCuZP+NIR group (treated by Rm-HCuZP and NIR irradiation). For the laser irradiation groups, 808 nm light (1 W/cm^2) was applied for 10 min after drug administration for 12 h. During the treatment period, the body weight and the tumor volume of mice were monitored every 2 days to assess the biosafety and therapeutic effect of Rm-HCuZP *in vivo*. The trend of weight change is illustrated in Figure 8b.

It can be observed that the mice's body weight over a span of 12 days shows minimal variation among the distinct treatment groups. Both the control group and the experimental groups maintained their body weights within a range of approximately 19.7 to 20.4 g. This could suggest that the prepared materials do not seem to cause significant adverse effects on the mice or demonstrate a level of biosafety specificity.

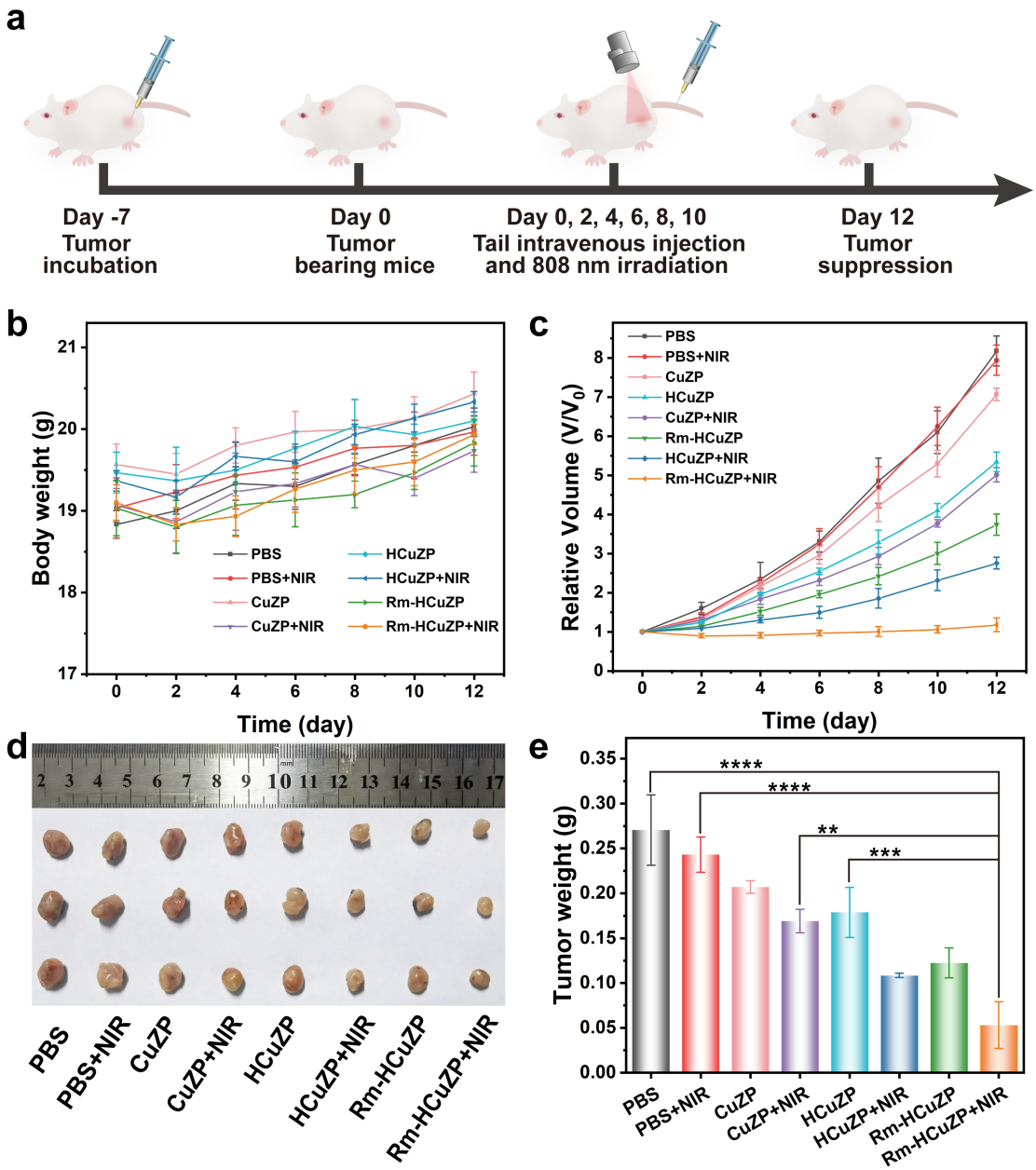

Figure 8. (a) Schematic illustration of the therapeutic study time line. (b) Variations in body weights in different treatments during the period. (c) Variations in the relative tumor volume in different groups. (d) Digital photos of tumors harvested from mice with different treatments for 12 days. (e) The weight of isolated tumors from the different groups after 12 days. The data for comparisons are shown to be significant, where *p < 0.05, **p < 0.01, *** p < 0.001, and **** p < 0.0001.

In addition, H&E staining was performed on the organs of mice, such as the heart, liver, spleen, lung, and kidney, for histological analysis (Figure S11). No

remarkable impairment or inflammation was observed in these organs compared with the control group, further confirming the biocompatibility and biosafety of the nanoformulations.

The trend of tumor volume change is shown in Figure 8c. Compared to the control groups (V/V_0 = 8), the growth rate of tumor volume is decelerated in all treatment groups, with the Rm-HCuZP+NIR experimental group (V/V_0 = 1.09) demonstrating the most pronounced inhibition of tumor growth. In addition, the weights and the corresponding digital photographs of excised tumors after sacrificing the mice also reveal the superior tumor-killing effect of the Rm-HCuZP+NIR group (Figure 8d and Figure 8e), with a tumor weight of 0.27 mg in the PBS group versus 0.053 mg in the Rm-HCuZP+NIR group. These results indicate that Rm-HCuZP with NIR provides an undeniable advantage in realizing the synergistic effects of multiple modalities of CDT/CT/PTT.

Subsequently, the H&E staining was used for histological analysis of the tumors (Figure 9a). Comparing the H&E staining results in different tumor tissue groups, it is observed that the tumor tissue treated with the Rm-HCuZP+NIR group reveals severe damage accompanied by the disappearance of nuclear lysis. However, the nuclear division phenomenon can still be clearly observed in the control group. Furthermore, TUNEL staining was used to investigate the apoptosis of tumor cells (blue for the normal cells, and green for the apoptosis cells) (Figure 9b). Relative to the control group, which shows strong blue fluorescence, the other experimental groups exhibit

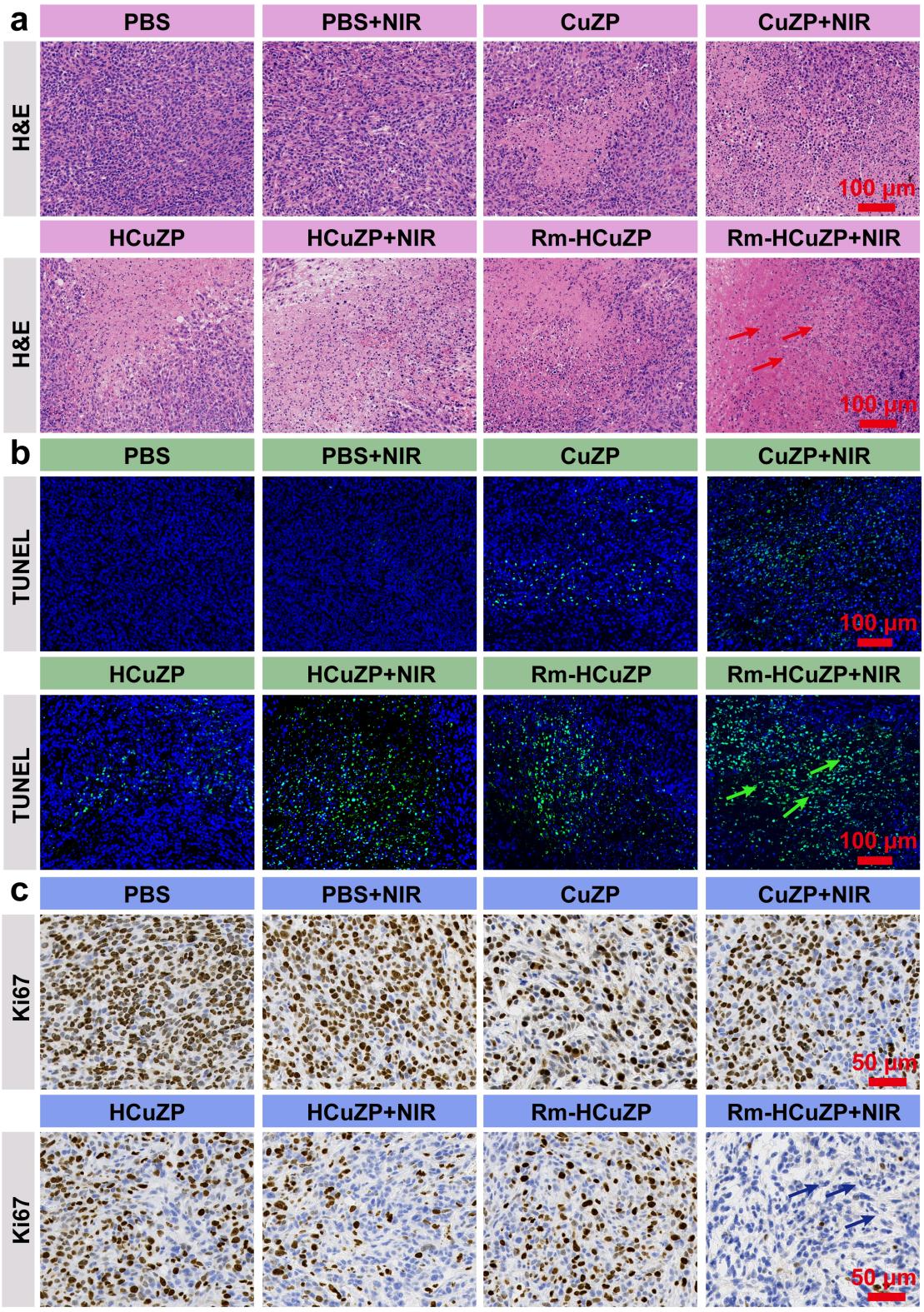

Figure 9. (a) H&E staining, (b) TUNEL staining and (c) Ki67 staining images of tumor tissues after different treatments for 12 days.

varying degrees of green fluorescence. Among them, the strongest green fluorescence is observed in the Rm-HCuZP+NIR group, implying the most severe apoptosis of

tumor cells. In addition, a similar tendency can be discovered from Ki67 staining (brown for cell proliferation, and blue for inhibition of cell growth). As shown in Figure 9c, the tumor tissue treated with Rm-HCuZP+NIR group displays the most prominent inhibition of tumor growth factor (stained in brown), while no significant inhibition of tumor cell proliferation is found in the control group. These results are sufficient to demonstrate that Rm-HCuZP upon NIR irradiation exhibits the ability to promote apoptosis and inhibit the growth of tumor cells, achieving a tumor killing effect.

4. CONCLUSIONS

In summary, a metal-organic framework-based bionic composite nanodrug (RBCM-HCPT@Cu/ZIF-8@PDA) is developed for synergistic treatment of breast cancer using CDT/CT/PTT therapy. Due to the surface coating of the erythrocyte membrane, Rm-HCuZP nanoformulations are endowed with the ability to prolong blood circulation, evade immune recognition, and enhance EPR effects, facilitating their aggregation at tumor sites. In addition, the acid-sensitive property of ZIF-8 realizes the effective release of copper ions and HCPT from the Rm-HCuZP nanoformulations within the tumor microenvironment, which can be conducive to overcoming the damage to normal tissues due to premature drug leakage, thus promoting safe and effective CDT/CT combination therapy. Moreover, the photothermal conversion performance of Rm-HCuZP nanoformulations can not only improve the efficiency of photothermal treatment of tumors, but also further enhance the effect of CDT therapy in inhibiting tumor growth through PTT-induced local

thermal therapy. The *in vitro* and *in vivo* studies demonstrate that erythrocyte membrane-camouflaged Rm-HCuZP nanoformulations show promise in synergistic CDT/CT/PTT therapy for potentially inhibiting tumor growth. This approach offers a therapeutic platform with potential biocompatibility and biosafety for improved combined CDT and chemical photothermal treatment targeting breast cancer.

Author contributions

L. R. and J. Z. produced composite nanoformulation and performed cell and animal experiments; L. R., Y. S. and G. J. analyzed the results and wrote the draft of manuscript; Y. S. and G. J. conceived the idea and designed the experiments; L. N. and A. S. provided suggestions and commented on the manuscript; K. E. Y., U. E. A. and S. O. S. reviewed the manuscript.

Declaration of Competing Interest

The authors declare that they have no known competing financial interests or personal relationships that could have appeared to influence the work reported in this paper.

Acknowledgments

This work was financially supported by the Huadong Medicine Joint Funds of the Zhejiang Provincial Natural Science Foundation of China under Grant No. LHDMZ23H300003 and the National Natural Science Foundation of China under Grant No. 51873194.

References

[1] P. Kumbhar, K. Kole, V. Khadake, P. Marale, A.i Manjappa, S. Nadaf, R. Jadhav, A. Patil, S. K. Singh, K. Dua, N. K. Jha, J. Disouza, V. Patravale, Nanoparticulate

drugs and vaccines: breakthroughs and bottlenecks of repurposing in breast cancer, J. Control. Release 349 (2022) 812-830.

[2] Y. Zhang, S. Tang, X. Feng, X. Li, J. Yang, Q. Liu, M. Li, Y. Chai, C. Yang, S. Lin, J. Liu, Tumor-targeting gene-photothermal synergistic therapies based on multifunctional polydopamine nanoparticles, Chem. Eng. J. 457 (2023) 141315.

[3] Z. Wang, Z. Li, Z. Sun, S. Wang, Z. Ali, S. Zhu, S. Liu, Q. Ren, F. Sheng, B. Wang, Y. Hou, Visualization nanozyme based on tumor microenvironment "unlocking" for intensive combination therapy of breast cancer, Sci. Adv. 6 (2020) eabc8733.

[4] C. Wang, W. Fan, Z. Zhang, Y. Wen, L. Xiong, X. Chen, Advanced nanotechnology leading the way to multimodal imaging-guided precision surgical therapy, Adv. Mater. 31 (2019) 1904329.

[5] Q. Chen, M. Zhang, H. Huang, C. Dong, X. Dai, G. Feng, L. Lin, D. Sun, D. Yang, L. Xie, Y. Chen, J. Guo, X. Jing, Single atom-doped nanosonosensitizers for mutually optimized sono/chemo-nanodynamic therapy of triple negative breast cancer, Adv. Sci. 10 (2023) 2206244.

[6] Y. Huang, Y. Jiang, Z. Xiao, Y. Shen, L. Huang, X. Xu, G. Wei, C. Xu, C. Zhao, Three birds with one stone: a ferric pyrophosphate based nanoagent for synergetic NIR-triggered photo/chemodynamic therapy with glutathione depletion, Chem. Eng. J. 380 (2020) 122369.

[7] M. Wang, G. J. Zhou, Y. J. Pan, Y. Xue, S. H. Zhu, Y. C. Yan, H. H. Yuan, S. B. Li, Q. L. Huang, Design and fabrication of cascade novel Fenton catalytic nanocomposite as theranostic agent for chemodynamic/photothermal synergistic tumor therapy, Mater. Design 219 (2022) 110794.

[8] D. Jana, D. D. Wang, A. K. Bindra, Y. Guo, J. W. Liu, Y. L. Zhao, Ultrasmall alloy nanozyme for ultrasoundand Near-Infrared light-promoted tumor ablation, ACS Nano 15 (2021) 7774-7782.

[9] L. J. Shao, T. S. Hu, X. Y. Fan, X. Z. Wu, F. F. Zhou, B. T. Chen, S. W. Tan, H. Xu, A. Q. Pan, S. Q. Liang, Y. J. He, Intelligent nanoplatform with multi therapeutic modalities for synergistic cancer therapy, ACS Appl. Mater. Interfaces

14 (2022) 13122-13135.

[10] N. Xu, A. Hu, X. M. Pu, J. Wang, X. M. Liao, Z. B. Huang, G. F. Yin, Cu-chelated polydopamine nanoparticles as a photothermal medium and ‘‘immunogenic cell death’’ inducer for combined tumor therapy, J. Mater. Chem. B 10 (2022) 3104-3118.

[11] Y. H. Shi, J. J. Zhang, H. Huang, C. Y. Cao, J. J. Yin, W. J. Xu, W. J. Wang, X. J. Song, Y. W. Zhang, X. C. Dong, Fe-doped polyoxometalate as acid-aggregated nanoplatform for NIR-II photothermal-enhanced chemodynamic therapy, Adv. Healthcare Mater. 9 (2020) 2000005.

[12] G. Song, Y. F. Sun, T. Q. Liu, X. Y. Zhang, Z. Y. Zeng, R. F. Wang, P. F. Li, C. H. Li, G. H. Jiang, Transdermal delivery of Cu-doped polydopamine using microneedles for photothermal and chemodynamic synergistic therapy against skin melanoma, Chem. Eng. J. 426 (2021) 130790.

[13] J. J. Ren, L. Zhang, J. Y. Zhang, W. Zhang, Y. Cao, Z. G. Xu, H. J. Cui, Y. J. Kang, P. Xue, Light-activated oxygen self-supplied starving therapy in near-infrared (NIR) window and adjuvant hyperthermia-induced tumor ablation with an augmented sensitivity, Biomaterials 234 (2020) 119771.

[14] X. Y. Zhang, G. H. Jiang, G. Song, T. Q. Liu, Y. F. Sun, Z. Y. Zeng, Fabrication of h-MnO_2@PDA composite nanocarriers for enhancement of anticancer cell performance by photochemical synergetic therapies. Front. Mater. Sci. 15(2) 2021 291-298.

[15] G. Song, G. H. Jiang, T. Q. Liu, X. Y. Zhang, Z. Y. Zeng, R. F. Wang, P. F. Li, Y. H. Yang, Separable microneedles for synergistic chemo-photothermal therapy against superficial skin tumors. ACS Biomater. Sci. Eng. 6(7) 2020 4116-4125.

[16] Y. Cheng, D. D. Bao, X. J. Chen, Y. J.Wu, Y. H. Wei, Z. B. Wu, F. Z. Li, J. G Piao, Microwave-triggered/HSP-targeted gold nano-system for triple-negative breast cancer photothermal therapy, Int. J. Pharm. 593 (2021) 120162.

[17] X. J. Chen, J. F. Zou, K. Zhang, J. J. Zhu, Y. Zhang, Z. H. Zhu, H. Y. Zheng, F. Z. Li, J. G. Piao, Photothermal/matrix metalloproteinase-2 dualresponsive gelatin nanoparticles for breast cancer treatment, Acta Pharm. Sin. B 11(1) (2021) 271-

282.

[18] C. Yang, M. R. Younis, J. Zhang, J. L. Qu, J. Lin, P. Huang, Programmable NIR-II photothermal-enhanced starvation-primed chemodynamic therapy using glucose oxidase-functionalized ancient pigment nanosheets, Small 16 (2020) 2001518.

[19] R. R. Fan, C. L. Chen, Huan Hou, D. Chuan, M. Mu, Z. Y. Liu, R. C. Liang, G. Guo, J. G. Xu, Tumor acidity and Near-Infrared light responsive dual drug delivery polydopamine-based nanoparticles for chemo-photothermal therapy, Adv. Funct. Mater. 31 (2021) 2009733.

[20] M. Khafaji, M. Zamani, M. Golizadeh, O. Bavi, Inorganic nanomaterials for chemo/photothermal therapy: a promising horizon on effective cancer treatment, Biophys. Rev. 11 (2019) 335-352.

[21] S. Q. Guan, X. J. Liu, Y. Fu, C. L. Li, J. X. Wang, Q. X. Mei, G. Y. Deng, W. R. Zheng, Z. P. Wan, J. Lu, A biodegradable ‘‘nano-donut” for magnetic resonance imaging and enhanced chemo/photothermal/chemodynamic therapy through responsive catalysis in tumor microenvironment, J. Colloid Interface Sci. 608 (2022) 344-354.

[22] Y. Shi, L. Y. Zeng, Y. B. Pan, H. Zhang, Z. Y. Wang, Y. H. Shi, A. G. Wu, Endo/exo-genous dual-stimuli responsive gold nanotetrapod-based nanoprobe for magnetic resonance imaging and enhanced multimodal therapeutics by amplifying ·OH generation, Acta Biomater. 154 (2022) 549-558.

[23] H. Shi, R. Wang, H. C. Cao, H. Y. Guo, P. Pan, C. F. Xiong, L. J. Zhang, Q. Yang, S. Wei, T. Liu, A metal-polyphenol-based oxygen economizer and Fenton reaction amplifier for self-enhanced synergistic photothermal/chemodynamic/chemotherapy, Adv. Healthcare Mater. 12 (2023) 2300054.

[24] Z. M. Xiao, W. B. Zuo, L. P. Chen, L. Wu, N. Liu, J. X. Liu, Q. Y. Jin, Y. L. Zhao, X. Zhu, H_2O_2 self-supplying and GSH-depleting nanoplatform for chemodynamic therapy synergetic photothermal/chemotherapy, ACS Appl. Mater. Interfaces 13 (2021) 43925-43936.

[25] Z. Y. Wang, Y. H. Shi, Y. Shi, J. H. Zhang, R. Hao, G. W. Zhang, L. Y. Zeng, Ultrasmall gold-coated mesoporous polydopamine nanoprobe to enhance chemodynamic therapy by self-supplying H_2O_2 and photothermal stimulation, ACS Appl. Mater. Interfaces 14 (2022) 54478-54487.

[26] L. Wang, Y. T. Xu, C. Liu, W. L. Si, W. J. Wang, Y. W. Zhang, L. P. Zhong, X. C. Dong, Y. X. Zhao, Copper-doped MOF-based nanocomposite for GSH depleted chemo/photothermal/chemodynamic combination therapy, Chem. Eng. J. 438 (2022) 135567.

[27] B. J. Ma, S. Wang, F. Liu, S. Zhang, J. Z. Duan, Z. Li, Y. Kong, Y. H. Sang, H. Liu, W. B. Bu, L. L. Li, Self-assembled copper−amino acid nanoparticles for in Situ glutathione "AND" H_2O_2 sequentially triggered chemodynamic therapy, J. Am. Chem. Soc. 141 (2019) 849-857.

[28] X. J. Di, Z. C. Pei, Y. X. Pei, T. D. James, Tumor microenvironment-oriented MOFs for chemodynamic therapy, Coord. Chem. Rev. 484 (2023) 215098.

[29] K. Cheng, B. Liu, X. S. Zhang, R. Y. Zhang, F. Zhang, G. Ashraf, G. Q. Fan, M. Y. Tian, X. Sun, J. Yuan, Y. D. Zhao, Biomimetic material degradation for synergistic enhanced therapy by regulating endogenous energy metabolism imaging under hypothermia, Nat. Commun. 13 (2022) 4567.

[30] S. Rojas, A. A. Vivo, P. Horcajada, Metal-organic frameworks: a novel platform for combined advanced therapies, Coord. Chem. Rev. 388 (2019) 202-226.

[31] C. S. Li, J. Ye, X. Yang, S. Liu, Z. Y. Zhang, J. Wang, K. F. Zhang, J. T. Xu, Y. J. Fu, P. P. Yang, Fe/Mn bimetal-doped ZIF-8-coated luminescent nanoparticles with up/downconversion dual-mode emission for tumor self-enhanced NIR-II imaging and catalytic therapy, ACS Nano 16 (2022) 18143-18156.

[32] B. B. Ding, H. Chen, J. Tan, Q. Meng, P. Zheng, P. A. Ma, J. Lin, ZIF-8 nanoparticles evoke pyroptosis for high-efficiency cancer immunotherapy, Angew. Chem. Int. Ed. 62 (2023) e202215307.

[33] X. Y.Meng, Z. X. Lu, Q. Y. Lv, Y. Q. Jiang, L. M. Zhang, Z. F. Wang, Tumor metabolism destruction via metformin-based glycolysis inhibition and glucose oxidase-mediated glucose deprivation for enhanced cancer therapy, Acta

Biomater. 145 (2022) 222-234.

[34] M. M. Li, R. Guo, J. J. Wei, M. Deng, J. X. Li, Y. Tao, M. Li, Q. He, Polydopamine-based nanoplatform for photothermal ablation with long-term immune activation against melanoma and its recurrence, Acta Biomater. 136 (2021) 546-557.

[35] H. W. Xu, Y. Zhang, H. T. Zhang, Y. R. Zhang, Q. Q. Xu, J. Y. Lu, S. P. Feng, X. Y. Luo, S. L. Wang, Q. F. Zhao, Siling Wang, Qinfu Zhao, Smart polydopamine-based nanoplatforms for biomedical applications: state-of-art and further perspectives, Coord. Chem. Rev. 488 (2023) 215153.

[36] X. Chu, L. F. Zhang, Y. L. Li, Y. He, Y. Zhang, C. Du, NIR Responsive doxorubicin-loaded hollow copper ferrit@polydopamine for synergistic chemodynamic/ photothermal/chemo-therapy, Small 19 (2023) 2205414.

[37] B. Liu, W. M. Wang, J. L. Fan, Y. Long, F. Xiao, M. Daniyal, C. Y. Tong, Q. Xie, Y. Q. Jian, B. Li, X. C. Ma, W. Wang, RBC membrane camouflaged prussian blue nanoparticles for gamabutolin loading and combined chemo/photothermal therapy of breast cancer, Biomaterials 217 (2019) 119301.

[38] Y. W. Zhao, Jine Wang, X. Cai, P. Ding, H. Y. Lv, R. J. Pei, Metal-organic frameworks with enhanced photodynamic therapy: synthesis, erythrocyte membrane camouflage, and aptamer-targeted aggregation, ACS Appl. Mater. Interfaces 12 (2020) 23697-23706.

[39] W. J. Liu, Y. Y. Huang, Cell membrane-engineered nanoparticles for cancer therapy, J. Mater. Chem. B 10 (2022) 7161-7172.

[40] S. Y. Zeng, Q. L. Tang, M. N. Xiao, X. Y. Tong, T. Yang, D. H. Yin, L. J. Lei, S. S. Li, Cell membrane-coated nanomaterials for cancer therapy, Mater Today Bio 20 (2023) 100633.

[41] F. Oroojalian, M. Beygi, B. Baradaran, A. Mokhtarzadeh, M. A. Shahbazi, Immune cell membrane-coated biomimetic nanoparticles for targeted cancer therapy, Small 17 (2021) 2006484.

[42] B. D. Zheng, M. T. Xiao, Red blood cell membrane nanoparticles for tumor phototherapy, Colloid Surf. B 220 (2022) 112895.

[43] C. Li, X. Q. Yang, J. An, K. Cheng, X. L. Hou, X. S. Zhang, Y. G. Hu, B. Liu, Y. D. Zhao, Red blood cell membrane-enveloped O_2 self-supplementing biomimetic nanoparticles for tumor imaging-guided enhanced sonodynamic therapy, Theranostics 10(2) (2020) 867-879.

[44] Y. F. Liu, N. C. Wen, K. Li, M. Q. Li, S. N. Qian, S. R. Li, T. Jiang, T. Wang, Y. W. Wu, Z. B. Liu, Photolytic removal of red blood cell membranes camouflaged on nanoparticles for enhanced cellular uptake and combined chemo-photodynamic inhibition of cancer cells, Mol. Pharmaceutics 19 (2022) 805-818.

[45] Y. H. Bao, J. F. Chen, H. Q. Qiu, C. Zhang, P. T. Huang, Z. W. Mao, W. J. Tong, Erythrocyte membrane-camouflaged PCN-224 nanocarriers integrated with platinum nanoparticles and glucose oxidase for enhanced tumor sonodynamic therapy and synergistic starvation therapy, ACS Appl. Mater. Interfaces 13 (2021) 24532-24542.

[46] T. Wu, T. Q. Lang, C. Zheng, W. L. Yan, Y. Li, R. Q. Zhu, X. Huang, H. A. Xu, Y. P. Li, Q. Yin, Promote intratumoral drug release and penetration to counteract Docetaxel-induced metastasis by photosensitizer-modified red blood cell membrane-coated nanoparticle, Adv. Funct. Mater. 33 (2023) 2212109.

[47] H. Y. Chu, J. W. Shen, C. Z. Wang, Y. M. Wei, Biodegradable iron-doped ZIF-8 based nanotherapeutic system with synergistic chemodynamic/photothermal/chemo-therapy, Colloids Surf. A Physicochem. Eng. Asp. 628 (2021) 127388.

[48] Z. X. Xie, S. Liang, X. C. Cai, B. B. Ding, S. S. Huang, Z. Y. Hou, P. A. Ma, Z. Y. Cheng, J. Lin, O_2-Cu/ZIF-8@Ce6/ZIF-8@F127 composite as a tumor microenvironment-responsive nanoplatform with enhanced photo-/chemodynamic antitumor efficacy, ACS Appl. Mater. Interfaces 11 (2019) 31671-31680.

[49] C. Q. Qiao, X. F. Wang, G. H. Liu, Z. Yang, Q. Jia, L. X. Wang, R. L. Zhang, Y. Q. Xia, Z. L. Wang, Y. Yang, Erythrocyte membrane camouflaged metal-organic framework nanodrugs for remodeled tumor microenvironment and enhanced tumor chemotherapy, Adv. Funct. Mater. 32 (2022) 2107791.

[50] J. Q. Li, R. X. Zhao, F. M. Yang, X. T. Qi, P. K. Ye, M. Xie, An erythrocyte membrane-camouflaged biomimetic nanoplatform for enhanced chemo-photothermal therapy of breast cancer, J. Mater. Chem. B 10 (2022) 2047.

[51] Y. Q. Miao, Y. T. Yang, L. M. Guo, M. S. Chen, X. Zhou, Y. G. Zhao, D. Nie, Y. Gan, X. X. Zhang, Cell membrane-camouflaged nanocarriers with biomimetic deformability of erythrocytes for ultralong circulation and enhanced cancer therapy, ACS Nano 16 (2022) 6527-6540.

[52] H. J. Wang, G. R. Williams, X. T. Xie, M. Wu, J. Z. Wu, L. M. Zhu, Stealth polydopamine-based nanoparticles with red blood cell membrane for the chemo-photothermal therapy of cancer, ACS Appl. Bio Mater. 3 (2020) 2350-2359.

[53] F. F. Zhang, C. L. Xin, Z. C. Dai, H. L. Hu, Q. An, F. Wang, Z. F. Hu, Y. Q. Sun, L. Tian, X. W. Zheng, Oncocyte membrane-camouflaged multi-stimuli-responsive nanohybrids for synergistic amplification of tumor oxidative stresses and photothermal enhanced cancer therapy, ACS Appl. Mater. Interfaces 14 (2022) 40633-40644.

[54] L. M. Ruan, G. Song, X. Y. Zhang, T. Q. Liu, Y. F. Sun, J. L. Zhu, Z. Y. Zeng, G. H. Jiang, Transdermal delivery of multifunctional CaO_2@Mn-PDA nanoformulations by microneedles for NIR-induced synergistic therapy against skin melanoma, Biomater. Sci. 9 (2021) 6830-6841.

[55] Q. Li, J. T. Yu, L. Lin, Y. L. Zhu, Z. X. Wei, F. Y. Wan, X. D. Zhang, F. He, L. L. Tian, One-pot rapid synthesis of Cu^{2+}-doped GOD@MOF to amplify the antitumor efficacy of chemodynamic therapy, ACS Appl. Mater. Interfaces 15 (2023) 16482-16491.

[56] J. Chang, L. F. Mo, J. F. Song, X. C. Wang, H. H. Liu, C. C. Meng, Y. J. Wu, A pH-responsive mesoporous silica nanoparticle-based drug delivery system for targeted breast cancer therapy, J. Mater. Chem. B 10 (2022) 3375-3385.

[57] B. B. Huang, Z. Tan, K. Bohinc, S. X. Zhang, Interaction between nanoparticles and charged phospholipid membranes, Phys. Chem. Chem. Phys. 20 (2018) 29249-29263.

[58] N. Liu, L. Wu, W. B. Zuo, Q. Lin, J. X. Liu, Q. Y. Jin, Z. M. Xiao, L. P. Chen, Y.

L. Zhao, J. Zhou, X. Zhu, pH/thermal-sensitive nanoplatform capable of on-demand specific release to potentiate drug delivery and combinational hyperthermia/chemo/chemodynamic Therapy, ACS Appl. Mater. Interfaces 14 (2022) 29668-29678.

[59] L. Jia, X. Li, H. Liu, J. D. Xia, X. Y. Shi, M. W. Shen, Ultrasound-enhanced precision tumor theranostics using cellmembrane-coated and pH-responsive nanoclusters assembled fromultrasmall iron oxide nanoparticles, Nano Today 36 (2021) 101022.

[60] Z. J. Xiong, Y. Wang, W. Zhu, Z. Ouyang, Y. Zhu, M. W. Shen, J. D. Xia, X. Y. Shi, A dual-responsive platform based on antifouling dendrimer-CuS nanohybrids for enhanced tumor delivery and combination therapy, Small Methods 2021 2100204.

[61] K.J. Zhou, H.M. Liu, S.R. Zhang, X.N. Huang, Y.G. Wang, G. Huang, B.D. Sumer, J.M. Gao, Multicolored pH-tunable and activatable fluorescence nanoplatform responsive to physiologic pH stimuli, J. Am. Chem. Soc. 134 (2012) 7803-7811.

[62] Q. Song, Y.J. Yin, L.H. Shang, T.T. Wu, D. Zhang, M. Kong, Y.D. Zhao, Y.Z. He, S.W. Tan, Y.Y. Guo, Z.P. Zhang, Tumor microenvironment responsive nanogel for the combinatorial antitumor effect of chemotherapy and immunotherapy, Nano Lett. 17 (2017) 6366-6375.

[63] W. T. Li, X. L. Zhou, S. K. Liu, J. L. Zhou, H. Ding, S. L. Gai, R. M. Li, L. Zhong, H. J. Jiang, P. P. Yang, Biodegradable nanocatalyst with self-supplying Fenton-like ions and H_2O_2 for catalytic cascade-amplified tumor therapy, ACS Appl. Mater. Interfaces 13 (2021) 50760-50773.

[64] H. J. Kong, Q. Chu, C. Fang, G. D. Cao, G. R. Han, X. Li, Cu-ferrocene-functionalized CaO_2 nanoparticles to enable tumor-specific synergistic therapy with GSH depletion and calcium overload, Adv. Sci. 8 (2021) 2100241.

[65] H. S.Hao, M. Yu, Y. F. Yi, S. J. Sun, X. Y. Huang, C. Y. Huang, Y. Q. Liu, W. X. Huang, J. Q. Wang, J. Zhao, M. Y. Wu, Mesoporous calcium peroxide-ignited NO generation for amplifying photothermal immunotherapy of breast cancer,

Chem. Eng. J. 437 (2022) 135371.

[66] X. N. Gao, Z. K. Jia, Y. Y. Cheng, M. Y. Ouyang, L. Feng, Y. Z. Wang, B. Tang, K. H. Xu, A pH-responsive cascade nanoplatform with circulating oxygen supply for collaborative breast cancer treatment, Chem. Commun. 58 (2022) 12090-12093.

[67] J. Shen, H. Z. Yu, Y. M. Shu, M. Ma, H. R. Chen, A robust ROS generation strategy for enhanced chemodynamic/photodynamic therapy via H_2O_2/O_2 self-supply and Ca^{2+} overloading, Adv. Funct. Mater. 31 (2021) 2106106.

[68] Y. F. Zhang, X. Y. Yue, S. C. Yang, X. L. Li, L. Cui, X. B. Cui, Y. Shi, Z. Y. Liu, X. H. Guo, Y. S. Li, Long circulation and tumor-targeting biomimetic nanoparticles for efficient chemo/photothermal synergistic therapy, J. Mater. Chem. B 10 (2022) 5035-5044.

[69] C. G. Wu, J. L. Liang, X. Wang, X. Y. Zhou, X. Cai, J. Xu, M. Wang, W. B. Wang, D. Ma, W. Xue, Light-activated nitric-oxide overproduction theranostic nanoplatform based on long-circulating biomimetic nanoerythrocyte for enhanced cancer gas therapy, Sci. China Chem. 10 (2021) 1796-1810.

[70] X. Q. Liu, W. Feng, H. J. Xiang, B. H. Liu, M. J. Ye, M. Wei, R. Dong, Y. Chen, K. R. Dong, Multifunctional cascade nanocatalysts for NIR-II-synergized photonic hyperthermia-strengthened nanocatalytic therapy of epithelial and embryonal tumors, Chem. Eng. J. 411 (2021) 128364.